A large Hα survey of star formation in relaxed and merging galaxy cluster environments at z ~ 0.15-0.3

Stroe, A.; Serrano Goncalves Sobral, D.R.; Paulino-Afonso, A.; Alegre, L.; Calhau, J.; Santos, S.; Weeren, R.J. van

Monthly Notices
of the
ROYAL ASTRONOMICAL SOCIETY

MNRAS **465,** 2916–2935 (2017)
Advance Access publication 2016 November 17

doi:10.1093/mnras/stw2939

A large Hα survey of star formation in relaxed and merging galaxy cluster environments at $z \sim 0.15$–0.3

Andra Stroe,[1★†] David Sobral,[2,3‡] Ana Paulino-Afonso,[4,5] Lara Alegre,[4,5] João Calhau,[2] Sergio Santos[2] and Reinout van Weeren[6]

[1]*European Southern Observatory, Karl-Schwarzschild-Str. 2, D-85748, Garching, Germany*
[2]*Department of Physics, Lancaster University, Lancaster LA1 4YB, UK*
[3]*Leiden Observatory, Leiden University, PO Box 9513, NL-2300 RA Leiden, the Netherlands*
[4]*Instituto de Astrofísica e Ciências do Espaço, Universidade de Lisboa, OAL, Tapada da Ajuda, P-1349-018 Lisbon, Portugal*
[5]*Departamento de Física, Faculdade de Ciências, Universidade de Lisboa, Edifício C8, Campo Grande, P-1749-016 Lisbon, Portugal*
[6]*Harvard Smithsonian Center for Astrophysics, 60 Garden Street, MS-06 Cambridge, MA 02138, USA*

Accepted 2016 November 10. Received 2016 November 10; in original form 2016 October 11

ABSTRACT

We present the first results from the largest Hα survey of star formation and active galactic nucleus activity in galaxy clusters. Using nine different narrow-band filters, we select >3000 Hα emitters within 19 clusters and their larger scale environment over a total volume of 1.3 $\times$ 10^5 Mpc^3. The sample includes both relaxed and merging clusters, covering the 0.15–0.31 redshift range and spanning from 5 $\times$ 10^{14} to 30 $\times$ 10^{14} M$_\odot$. We find that the Hα luminosity function for merging clusters has a higher characteristic density ϕ^* compared to relaxed clusters. ϕ^* drops from cluster core to cluster outskirts for both merging and relaxed clusters, with the merging cluster values ∼0.3 dex higher at each projected radius. The characteristic luminosity L^* drops over the 0.5–2.0 Mpc distance from the cluster centre for merging clusters and increases for relaxed objects. Among disturbed objects, clusters hosting large-scale shock waves (traced by radio relics) are overdense in Hα emitters compared to those with turbulence in their intracluster medium (traced by radio haloes). We speculate that the increase in star formation activity in disturbed, young, massive galaxy clusters can be triggered by interactions between gas-rich galaxies, shocks and/or the intracluster medium, as well as accretion of filaments and galaxy groups. Our results indicate that disturbed clusters represent vastly different environments for galaxy evolution compared to relaxed clusters or average field environments.

Key words: galaxies: clusters: general – galaxies: evolution – galaxies: formation – galaxies: luminosity function, mass function – large-scale structure of Universe.

1 INTRODUCTION

Since the dawn of the first stars and the first galaxies up to the present age, there has been tremendous evolution in galaxy populations (e.g. Lilly et al. 1996; Madau et al. 1996; Hopkins & Beacom 2006; Madau & Dickinson 2014). Star formation (SF) activity steadily rose up to $z \sim 2$–3, but has been declining since then (Lilly et al. 1996; Karim et al. 2011; Sobral et al. 2013; Stroe & Sobral 2015). This evolution is reflected in the properties of star-forming galaxies: the typical star formation rate (SFR) of galaxies (SFR*) at $z \sim 2$ is a factor ∼10 higher than in the local Universe (e.g. Sobral et al. 2013, 2014), while the specific SFR (sSFR) of galaxies at fixed mass increases with redshift by approximately the same amount (e.g. Fumagalli et al. 2012; Koyama et al. 2013; Sobral et al. 2014). Half of the stellar mass observed today was formed before $z \sim 1$, when the Universe was about a third of its current age (e.g. Marchesini et al. 2009; Muzzin et al. 2013; Madau & Dickinson 2014).

The properties of galaxies do not only vary with cosmic time, but also with environment (e.g. Peng et al. 2010, 2012; Darvish et al. 2016). There is a strong correlation between local density and the properties of the galaxy population. At $z < 1$, massive elliptical galaxies are located at the centres of virialized clusters. Additionally, the general galaxy population in these clusters is dominated by passive, ellipticals and S0s (Dressler 1980a,b; Dressler et al. 1997). The fraction of star-forming galaxies increases with radius from the cluster centre towards the cluster outskirts. The star-forming

★ E-mail: astroe@eso.org
† ESO Fellow.
‡ VENI Fellow.

fraction is even higher in the large-scale array of filaments surrounding clusters and in properly isolated field galaxies (Dressler 1980b). Typical cluster environments prevent formation of new stars, either by maintaining galaxies quenched or by accelerating quenching processes (e.g. Butcher & Oemler 1978a,b; Dressler 1980b). Environmental quenching is so effective that, at low redshifts ($z < 0.1$), the fraction of star-forming galaxies within relaxed clusters is below that in blank fields as far as three times the virial radius of the clusters (Chung et al. 2011). Therefore, despite the high density of galaxies within clusters, the number density of star-forming galaxies is lower in clusters than in average fields (e.g. Dressler 1980b; Goto et al. 2003). The potential transformation of field spirals into cluster ellipticals and S0s has been attributed to a number of processes: ram pressure stripping of the gas content infalling galaxies by the intracluster medium (ICM, e.g. Gunn & Gott 1972; Fumagalli et al. 2014), gas removal (strangulation, Larson, Tinsley & Caldwell 1980) and truncation of the halo and disc (harassment, Moore et al. 1996) by tidal forces caused by interactions with other cluster galaxies or by gradients in the cluster gravitational potential.

So far, most studies have focused on field galaxies or on galaxies in relaxed clusters. However, less literature has been dedicated to intermediate-density environments, such as filaments, and non-relaxed clusters, which provide a very different environment for the galaxies to interact with, compared to relaxed clusters. Filamentary structures and the outskirts of merging clusters host shock waves with Mach numbers between ∼3 and ∼10 (Pfrommer et al. 2006; Vazza et al. 2011; Beck, Dolag & Donnert 2016), while the more central areas of merging clusters have increased turbulence. Recent studies indicate that non-relaxed clusters might display a reversal of the typical relaxed cluster environmental trends (Stroe et al. 2014a, 2015a). For example, star-forming tails and Hα emitting galaxies were found near the shocks in the clusters Abell 2744 (Owers et al. 2012) and Abell 521 (Ferrari et al. 2003; Umeda et al. 2004). Abell 2384 hosts an unexpected population of disc galaxies towards the cluster core (Pranger et al. 2014). Similarly, Boschin et al. (2004) find a significant population of active galaxies in the dynamically young cluster Abell 2219. Darvish et al. (2014) find a higher fraction of Hα emitting galaxies in filaments than in other environments. These galaxies are more metal rich and have lower interstellar medium electron densities than their field counterparts (Darvish et al. 2015). The young massive merging cluster CIZA J2242.8+5301 ('Sausage' cluster, Kocevski et al. 2007) was found to host a large population of star-forming galaxies and active galactic nucleus (AGN) with high SFR, increased metallicity, lower electron densities (similar to filaments) and winds (Stroe et al. 2014a, 2015a; Sobral et al. 2015). The similarly massive 1RXS J0603.3+4214 cluster ('Toothbrush', van Weeren et al. 2012) was found to be devoid of star-forming galaxies, an effect which may be attributed to the longer period passed since the subclusters merged (2 Gyr for the 'Toothbrush' compared to <1 Gyr for the 'Sausage'; Stroe et al. 2015a).

A range of SF tracers can be used to track the continuous transformation of galaxies across cosmic time and environment (e.g. Madau & Dickinson 2014). However, different tracers are sensitive to different time-scales, leading to different selection functions. Comparing studies performed with different SF tracers can result in contradicting conclusions regarding the SF evolution with cosmic time and environment. Many surveys of both clusters and fields (e.g. Balogh et al. 1999, 2004; Lilly et al. 2007; Barrena et al. 2011; Cohen et al. 2014; Le Fèvre et al. 2015) use deep spectroscopy to study the SF properties of galaxies selected based on broad-band (BB) photometry. Such surveys provide unique insight into the detailed physical processes of the surveyed galaxies. However, spectroscopic surveys have complicated selection functions, which, in many cases, do not only depend on the mass or SFR of the galaxies, but suffer from constrains in placement of fibres/slits. Achieving spectroscopic completeness is particularly difficult for clusters of galaxies, where the density of sources is very high and taking a spectrum for each galaxy requires numerous pointings with different fibre/slit placements. Candidate cluster members are most easily selected for spectroscopic follow-up through the red-sequence method, which ensures the galaxies are selected around the right redshift range. However, this method is biased against star-forming galaxies, selecting, by design, passive galaxies. Therefore, one of the main challenges is to obtain comparable samples of star-forming galaxies at different redshifts and in a range of environments, uniformly selected down to the same SFR limit.

An efficient technique to uniformly select galaxies undergoing recent SF (averaged over ∼10–20 Myr) is to use the narrow-band (NB) technique to trace Hα emission within a small redshift range (e.g. Bunker et al. 1995). A NB filter which captures Hα emission as well as the stellar continuum is used in combination with a BB filter which is dominated by stellar continuum. By subtracting the BB from the NB, emission line systems can be easily uncovered. This technique is ideal for selecting field star-forming galaxies at many different narrow redshift slices within which not much evolution is expected. The NB technique is also very well suited for identifying emission-line systems in clusters, ensuring selection of all cluster members within the plane of the sky as well as in the redshift direction (e.g. Iglesias-Páramo et al. 2002; Kodama et al. 2004; Matsuda et al. 2011; Sobral et al. 2011; Koyama et al. 2013; Stroe et al. 2014a).

As mentioned before, violent merging clusters and filamentary environments are expected to lead to a different evolution for galaxies than relaxed clusters. It is therefore important to quantify the nature and evolution of galaxies in the largely unexplored parameter space of merging and relaxed clusters as well as the cosmic web around them. These low- and mid-redshift ($z \sim 0.1$–0.7) disrupted environments might be very similar to high-redshift ($z \sim 1$–5) clusters and protoclusters, and can therefore serve as ideal counterparts to easily study. Pilot analyses of the 'Sausage' and 'Toothbrush' merging clusters (Stroe et al. 2014a, 2015a; Sobral et al. 2015) indicate that shocks in young mergers may induce SF in merging cluster galaxies. Could the turbulence also lead to enhanced SF? Could the different merger histories of clusters play a significant role? What is the dependence of SF on the mass of the host cluster? Is the merging activity more important than the mass of the cluster? The dense cluster environments likely disrupt/quench small galaxies and in turn strongly affect the faint-end slope of the luminosity function (LF).

To address these questions, we started an Hα NB observing campaign to study the large-scale structure around a statistically significant set of 19 low-redshift ($0.15 < z < 0.31$) clusters sampling a range of masses, luminosities and relaxation states. In this first paper, we present the cluster sample, the survey strategy, data collection and reduction. We also discuss Hα LFs for different redshift bins, cluster merger states, masses, X-ray luminosities as well as for different environments in and around the clusters.

The paper is organized in the following way: in Section 2, we present the sample of clusters and their properties; in Section 3, we discuss the NB and corresponding subtraction BB observations and their reduction, as well as any ancillary data we are using. Section 4 covers the Hα emitter selection, while in Section 5, we present the formalism of obtaining LFs. In Section 6, we present the

Table 1. List of targets with coordinates, redshift, X-ray luminosity, mass (M_{200} estimated from weak lensing when available or total mass computed from the cluster's velocity dispersion σ) and relaxation state.

Field	RA hh mm ss	Dec. ° ′ ″	z	$L_{X,0.1-2.4\,keV}$ (10^{44} erg s^{-1})	M_{200} WL (10^{14} M$_\odot$)	M_{total} σ (10^{14} M$_\odot$)	State
A1689	$13^h11^m29^s$	$-01°20'17''$	0.183	14	18^{+4}_{-3}	20^{+5}_{-3}	Relaxed
A963	$10^h17^m13^s$	$+39°01'31''$	0.206	6	$7.6^{+1.5}_{-1.3}$	–	Relaxed
A1423	$11^h57^m17^s$	$+33°36'37''$	0.213	6	$4.6^{+1.2}_{-1.0}$	–	Relaxed
A2261	$17^h22^m27^s$	$+32°07'58''$	0.224	11	$12.7^{+2.3}_{-1.5}$	–	Relaxed
A2390	$21^h53^m35^s$	$+17°41'12''$	0.228	13	$11.1^{+1.9}_{-1.7}$	–	Relaxed, mini-halo
Z2089	$09^h00^m36^s$	$+20°53'39''$	0.2343	7	∼5		Relaxed
RXJ2129	$21^h29^m38^s$	$+00°05'39''$	0.235	12	$5.3^{+1.8}_{-1.4}$	–	Relaxed, mini-halo
RXJ0437	$04^h37^m10^s$	$+00°43'38''$	0.285	9	∼5	–	Relaxed
A545	$05^h32^m23^s$	$-11°31'50''$	0.154	5	–	11–18	Halo
A3411	$08^h41^m54^s$	$-17°29'05''$	0.169	5	–	23–37	Relic
A2254	$17^h17^m40^s$	$+19°42'51''$	0.178	5	–	15–29	Halo
'Sausage'	$22^h42^m50^s$	$+53°06'30''$	0.188	7	25.1 ± 5.3	∼30	Relic
A115	$00^h55^m59^s$	$+26°22'41''$	0.1971	9	$6.7^{+3.2}_{-2.1}$	–	Relic
A2163	$16^h15^m34^s$	$-06°07'26''$	0.203	38	$29.0^{+4.6}_{-5.8}$	39 ± 4	Halo
A773	$09^h17^m59^s$	$+51°42'23''$	0.217	6	$10.2^{+1.5}_{-1.3}$	12–27	Halo
'Toothbrush'	$06^h03^m30^s$	$+42°17'30''$	0.225	8	$9.6^{+2.1}_{-1.5}$	∼22	Relic, halo
A2219	$16^h40^m21^s$	$+46°42'21''$	0.2256	12	$10.9^{+2.2}_{-1.8}$	–	Halo
A1300	$23^h23^m07^s$	$+01°43'16''$	0.3072	13	–	∼6	Halo, relic
A2744	$00^h14^m18^s$	$-30°23'22''$	0.308	13	20.6 ± 4.2	–	Halo, relic

different Hα LFs for clusters and the fields around them binned by cluster mass, luminosity, redshift, merger stage etc. In Section 7, we discuss the implications of our results for the cosmic evolution of cluster and field galaxies. The conclusions can be found in Section 8.

We assume a flat Λ cold dark matter cosmology, with $H_0 = 70$ km s^{-1} Mpc^{-1}, matter density $\Omega_M = 0.3$ and dark energy density $\Omega_\Lambda = 0.7$. We have made use of the online cosmology calculator presented in Wright (2006), as well as its PYTHON implementation. Images are in the J2000 coordinate system. Magnitudes are in the AB system. We use a Chabrier initial mass function (IMF; Chabrier 2003).

2 CLUSTER SAMPLE

Our sample of 19 clusters was selected mainly to probe a range in redshift ($0.15 < z < 0.31$), mass, luminosity and merger states. Our sample includes relaxed and merging clusters hosting increased turbulence and shock waves (see Fig. 1). Increased turbulence in the ICM is indicated by the presence of diffuse radio emission co-located with the ICM (halo, Feretti et al. 2012). ICM shocks, thought to be produced at the merger of two massive clusters, can lead to particle acceleration which in the presence of magnetic fields leads to radio synchrotron emission (relics, Feretti et al. 2012). ICM shocks can also be detected as temperature or density discontinuities in the ICM, using X-ray data (e.g. Markevitch et al. 2002). Theory predicts that as the clusters pass through each other, the shocks are produced first, hence the relics are visible first. The merger also induces large bulk motions, which take time to cascade down to small-scale (10–100 kpc) turbulence capable of re-accelerating electrons and hence produce a radio halo (e.g. Donnert et al. 2013; Brunetti & Jones 2014). Therefore, on average, mergers with relics only could be younger than disturbed clusters hosting a halo+relic or a halo only. Even some relaxed clusters can show some degree of disturbance at their cores: gas sloshing around the central radio galaxy in turn generates turbulence. This turbulence can re-accelerate plasma from the radio galaxy to form extended diffuse radio emission, called a mini-halo (ZuHone et al. 2010; Feretti et al. 2012).

Details about each cluster can be found in Appendix A, and the main physical properties can be found summarized in Table 1 and visualized in Fig. 1. The targets are separated in relaxed and merging, and presented in increasing redshift order.

3 DATA, OBSERVATIONS AND DATA REDUCTION

3.1 Ancillary data

Our targets have useful ancillary data in the form of additional targeted or public survey photometry or spectroscopic redshifts. Note however that the photometry and spectroscopy availability and quality is highly dependent on the field, thus resulting in inhomogeneous ancillary data.

Many of the clusters are covered by the Sloan Digital Sky Survey (SDSS) in its 9th data release (SDSS DR9; Abazajian et al. 2009). For A2744, we employ the VLT Survey Telescope ATLAS survey data available in the g, r, i and z bands (Shanks et al. 2015). Four clusters have fully reduced and stacked images produced using the MegaPipe image stacking pipeline which are made available through Terapix.[1] We also employ g, r, i Subaru images of A3411 presented in van Weeren et al. (2017). We downloaded BB data

[1] A545: g, r, i, z bands, PI Morrison, ID 05BH42; A1300: g, r bands, PI Richard, ID 13AF05; A2163: g, r bands, PI Hoekstra, 05AC10; RXJ2129: g, r, i bands, PI Kneib, 10BF23 and PI Rogerson, 12BC31.

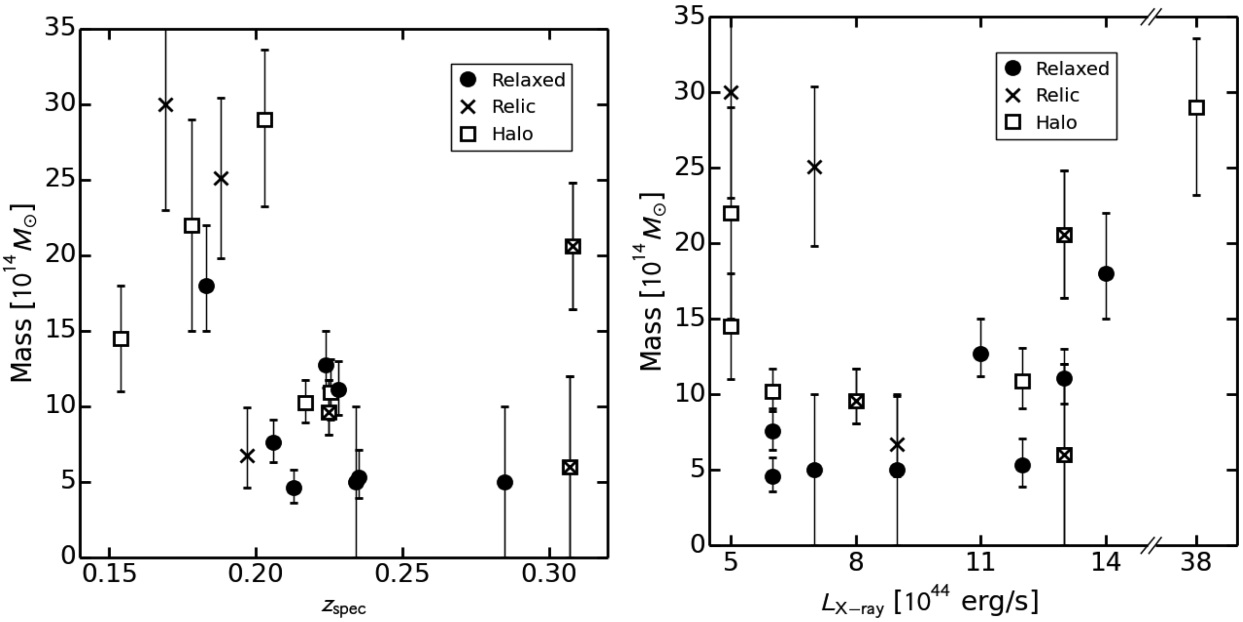

Figure 1. Distribution of galaxy clusters with respect to mass and redshift (left-hand panel) and with respect to mass and X-ray luminosity (right-hand panel). The relaxation state is encoded in the symbol. Note that masses are inferred from weak lensing estimates when available, but in some cases such an estimate was not available so we use the total mass estimate based on the cluster's velocity dispersion. Note the lack of correlation between mass and luminosity, especially for the disturbed clusters.

Table 2. List of targets with the luminosity distance (D_L), NB and BB filters used, the effective NB observing time, as well as observing period. The final column lists the volume in each field, amounting to a total volume of 1.3×10^5 Mpc^3.

Field	D_L (Mpc)	NB filter (Hα)	BB filter (rest-frame R)	NB Eff. int. time (ks)	Obs. period	Volume (10^4 Mpc^3)
A1689	887.8	NOVA7743	WFCSloanI	14.6	2016 June	4.3
A963	1013	NOVA7941	WFCSloanI	12.6	2016 March, April	5.9
A1423	1051.6	NOVA7941	WFCSloanI	13.8	2016 March, April	6.0
A2261	1110.5	NOVA804HA	WFCSloanI	12	2015 July	5.0
A2390	1133	NOVA804HA	WFCSloanI	15	2015 July	4.8
Z2089	1168.6	NOVA8089	WFCSloanI	18	2012 October, 2013 November	7.3
RXJ2129	1103.6	NOVA8089	SDSS *i*	7	2016 June	7.1
RXJ0437	1462.5	MB837	BBIc	18	2014 December	14.1
A545	731.3	MB753	CFHT *i*	18	2014 December	3.7
A3411	808.7	MB770	Subaru *i*	18	2014 December	4.3
A2254	858.3	NOVA7743	WFCSloanI	15	2015 July	4.5
'Sausage'	867.7	NOVA782HA	WFCSloanI	47.4	2012 October, 2013 November	3.4
A115	961.6	NOVA782HA	SDSS *i*	16.8	2015 October, November	3.6
		NOVA7941	–	10.2	–	5.8
		NOVA7743	–	11.4	–	4.2
A2163	996.5	NOVA7941	WFCSloanI	26.3	2016 March, April, June	6.1
A773	1012.4	NOVA7941	WFCSloanI	7.8	2015 November	6.0
'Toothbrush'	1118.5	NOVA804HA	WFCSloanI	51	2012 October, 2013 November	4.6
A2219	1119.6	NOVA804HA	WFCSloanI	12	2015 July	4.9
A1300	1595.2	MB856	BBIc	18	2014 December	11.5
A2744	1600	MB856	BBIc	18	2014 December	10.9

available from the Isaac Newton Telescope (INT) and European Southern Observatory (ESO)/MPG 2.2m archives and reduced in the manner described below in Section 3.3. For A115 and RXJ2129, we used the SDSS *i*-band data for BB subtraction mosaicked through MONTAGE,[2] which we processed in the same way as all of the other data (see Section 3.3).

For near-infrared (NIR) bands, we make use of data from the Visible and Infrared Survey Telescope for Astronomy (VISTA) Hemisphere Survey (VHS; Edge et al. 2013) and the VISTA Kilo-degree Infrared Galaxy Survey (VIKING; McMahon et al. 2013), as well as the United Kingdom Infra-Red Telescope (UKIRT) Infrared Deep Sky Survey data (UKIDSS; Lawrence et al. 2007). When such deep data are not available, we explore all sky NIR data from the Two Micron All Sky Survey (2MASS, Skrutskie et al. 2006).

[2] http://hachi.ipac.caltech.edu:8080/montage/index.html

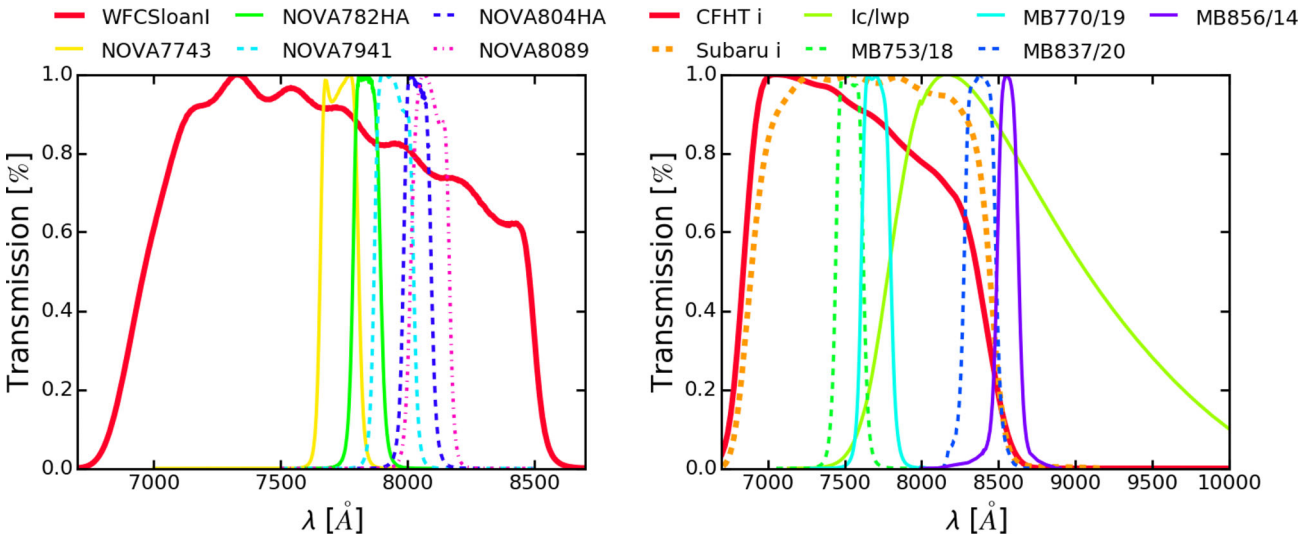

Figure 2. Normalized profiles of the NB filters used to survey Hα emitters at the redshift of our clusters. The BB filters used for continuum subtraction are also overplotted.

We collect redshifts available from targeted studies on particular clusters in our samples (Lemonon et al. 1997; Pierre et al. 1997; Boschin et al. 2004; La Barbera et al. 2004; Barrena et al. 2007a,b; Frye et al. 2007; Maurogordato et al. 2008; Barrena et al. 2011; Girardi et al. 2011; Owers et al. 2011; Coe et al. 2012; Houghton et al. 2012; Ziparo et al. 2012; Lemze et al. 2013; Dawson et al. 2015; Sobral et al. 2015; Jee et al. 2016; van Weeren et al. 2017). We also make use of the redshift compilation from Rines et al. (2013) and the 2dF Galaxy Redshift Survey (2dFGRS; Colless et al. 2001). Note however that most of these studies specifically targeted the passive galaxy population, thus we do not necessarily expect overlap with the sources we will select as Hα emitters. Additionally, we do not have many redshifts for sources at other than the cluster redshift. However, these data are useful to check the reliability of our star-forming galaxy selection methods (i.e. galaxies confirmed as passive with spectroscopy should not be selected as Hα emitters). The spectroscopic redshifts are used in Section 4.

3.2 New Hα NB and associated BB observations

We acquired NB data tracing Hα emission in the field and at the redshift of each cluster, as well as associated BB observations. The survey is designed to capture a sufficiently large field of view (FOV, $\sim$0.5 deg^2) in a single exposure to avoid inhomogeneities caused by mosaicking. At full depth, the survey reaches galaxies a few orders of magnitude fainter than typical Hα emitters, whilst still capturing the brightest Hα emitters. We targeted clusters to match existing NB filters mounted on wide-field cameras (WFCs). Additionally, we built custom made NB filters to cover specific redshift slices, optimized to capture Hα emission at the redshift of a few clusters. We compare the redshift range covered by the clusters given their velocity dispersion σ and find all clusters but A2163 are fully covered within 1.644σ from the central redshift. Within this 1.664σ range, we encompass 90 per cent of cluster galaxies and the cut will happen only at one side of the distribution. Therefore, for all clusters but A2163 we cover at least 95 per cent of the cluster line emitters. Because of its high mass and large velocity dispersion, the lower redshift distribution of A2163 galaxies is not fully covered by the NB filter. The filter covers down to -1σ. This amounts to covering at least 85 per cent of cluster sources. Therefore, as per our design, the filters cover very well the redshift distribution of clusters.

Table 3. Filter effective central wavelength and full width at half-maximum (FWHM) for the filters used in this study.

Telescope	Filter	λ_c (Å)	FWHM (Å)
INT	NOVA7743	7731.9	152.5
	NOVA782HA	7838.8	110.0
	NOVA7941	7944.5	155.0
	NOVA804HA	8037.7	110.5
	NOVA8089	8086.7	152.5
	WFCHARB	4361.2	1020.0
	WFCHARR	6505.6	1405.0
	WFCSloanI	7671.3	1510.0
MPG 2.2	MB753	7530.4	182.5
	MB770	7704.1	192.5
	MB837	8377.6	210.0
	MB856	8557.8	144.0
	BBIc	8299.7	1283.8
CFHT	*u*	3798.7	700.0
	g	4861.0	1430.0
	e	6260.1	1220.0
	I	7577.4	1520.0
	z	8876.2	870.0
Subaru	*g*	4794.2	1174.3
	r	6263.2	1414.4
	I	7666.5	1542.5
SDSS	*g*	4640.4	1158.4
	r	6122.3	1111.2
	I	7439.5	1044.6
	z	8897.1	1124.6

3.2.1 *Isaac Newton Telescope data*

For the northern targets, we used the WFC[3] mounted on the 2.5-m INT.[4] The WFC consists of four CCDs (pixel scale of

[3] http://www.ing.iac.es/engineering/detectors/ultra_wfc.htm
[4] http://www.ing.iac.es/Astronomy/telescopes/int/

0.333 pixel arcsec^{-1}) forming a 0.56 × 0.56 deg^2 with the top-right (NW on the sky) corner missing, with chip gaps of ∼20 arcsec. The observations were taken in a five-point dither pattern to cover the chip gaps.

Data were taken over a total of 16 nights, between 2015 July and 2016 June, with a variety of moon phases (eight dark, three grey and five bright nights) and observing conditions (seeing of 0.8–2.0 arcsec). We took 600 s individual exposures in the NB filters and 200 s exposures on the BB filters, to avoid saturation of bright objects. This strategy enables us to identify bright emitters as well as avoid sky area loss because of saturation haloes and spikes around bright stars. To this, we are also adding data on the 'Sausage' and 'Toothbrush' clusters presented in Stroe et al. (2014a, 2015a). For many clusters, the observations were taken months apart which allows the removal of variable and moving sources through stacking.

For each cluster, we obtained data in one NB filter chosen to cover the Hα emission redshifted at the distance of each galaxy cluster. The only exception is A115, where we took NB observation in three NB redshift slices to cover the Hα emission in sources in the foreground, inside and in the background of the cluster. We used the already existing custom-made NB filters presented in Stroe et al. (2014a), NOVA782HA and NOVA804HA. We also bought new custom-made filters (NOVA7743, NOVA7941 and NOVA8089) of about 150 Å width. A total of five separate NB filters were used for this study. With our five filters, we have continuous Hα coverage between $z \sim 0.166$ and $z \sim 0.244$.

The details of the NB filters and other BB filter data we employed can be found in Table 3 and Fig. 2. The filter profiles have been convolved with the quantum efficiency of the CCD and the effect of the optics. In case of the clusters observed with the INT, we obtained data in the WFCSloanI filter to measure the continuum emission. For A115, we used SDSS images to extract sources for BB subtraction in the same way as all the other images. The exact filters used as NB and BB for broad emission subtraction for each cluster are listed in Table 2.

3.2.2 *ESO2.2m telescope data*

For the southern targets, we used the Wide Field Imager (Baade et al. 1999) on the ESO/MPG 2.2m telescope.[5] Eight individual $2k \times 4k$ CCDs (with 0.238 arcsec pixel scale) form the detector, with 14 and 23 arcsec chip gaps in the NS and EW directions, respectively. A seven-point dither pattern was employed obtain contiguous sky coverage across the chip gaps.

The data were taken in excellent seeing conditions (0.4–0.6 arcsec) in 2014 December, under dark skies using four different NB filters to match the redshifts of the clusters. With the NB filters we cover the 0.133–0.189 redshift range and the 0.260–0.315 range. As with the INT data, NB filter exposures were 600 s, with 200 s for the BB. Observations in the filter BBIc were taken for BB subtraction. However, in the case of some clusters, this filter is too red, so Canada–France–Hawaii Telescope (CFHT) (available from Terapix) and Subaru (van Weeren et al. 2017) *i*-band images were used. Table 2 lists the details of NB and BB filters which were used for each cluster.

3.3 Hα NB and associated BB data reduction

We reduced the NB and BB data using our data reduction pipeline implemented in PYTHON (Stroe et al. 2014a), in combination with the ASTROMATIC[6] software package, specifically SEXTRACTOR (Bertin & Arnouts 1996), SCAMP (Bertin 2006), SWARP (Bertin et al. 2002) and MISSFITS (Marmo & Bertin 2008).

Table 4. Clusters with NB and BB filters. Average 3σ limiting magnitudes (measured in 5 arcsec apertures) for the different fields in the NB and BB. The limits are calculated per chip and we report the average. We also add a standard deviation of these limits, which is calculated between the values obtained for the different chips. We also report the limiting Hα luminosity at 50 per cent completeness, as well as the total number of emitters selected in each field.

Field	Filter	Avg. 3σ (mag)	Std. dev. 3σ (mag)	Lim. log L (erg s^{-1})	No. emit.
A1689	NOVA7743	20.16	0.05	40.2	291
	WFCSloanI	19.81	0.07	–	–
A963	NOVA7941	20.16	0.03	40.5	100
	WFCSloanI	21.23	0.08	–	–
A1423	NOVA7941	20.12	0.07	40.4	193
	WFCSloanI	21.12	0.08	–	–
A2261	NOVA804HA	19.95	0.03	40.5	361
	WFCSloanI	19.89	0.04	–	–
A2390	NOVA804HA	20.2	0.04	40.4	258
	WFCSloanI	20.52	0.07	–	–
Z2089	NOVA8089	18.83	0.03	41.2	67
	WFCSloanI	20.39	0.10	–	–
RXJ2129	NOVA8089	19.64	0.03	41.0	130
	i	19.73	–	–	–
RXJ0437	MB837	19.53	0.04	41.0	293
	BBIc	19.35	0.05	–	–
A545	MB753	19.75	0.07	40.4	148
	i	20.66	–	–	–
A3411	MB770	19.93	0.05	40.5	410
	i	21.81	–	–	–
A2254	NOVA7743	20.59	0.05	40.2	391
	WFCSloanI	21.31	0.02	–	–
'Sausage'	NOVA782HA	18.94	0.20	40.7	201
	WFCSloanI	19.08	0.19	–	–
A115	NOVA782HA	19.57	0.07	40.6	144
	NOVA7941	18.86	0.05	41.0	56
	NOVA7743	19.08	0.06	41.0	68
	i	19.71	–	–	–
A2163	NOVA7941	19.24	0.08	40.7	146
	WFCSloanI	20.12	0.04	–	–
A773	NOVA7941	19.17	0.05	41.0	140
	WFCSloanI	19.67	0.05	–	–
'Toothbrush'	NOVA804HA	20.03	0.08	40.4	463
	WFCSloanI	20.58	0.06	–	–
A2219	NOVA804HA	20.17	0.05	40.4	536
	WFCSloanI	20.60	0.06	–	–
A1300	MB856	19.52	0.08	40.9	890
	BBIc	19.20	0.35	–	–
A2744	MB856	19.52	0.09	40.7	619
	BBIc	19.48	0.07	–	–

[5] http://www.mpia.de/science/2dot2m

[6] www.astromatic.net

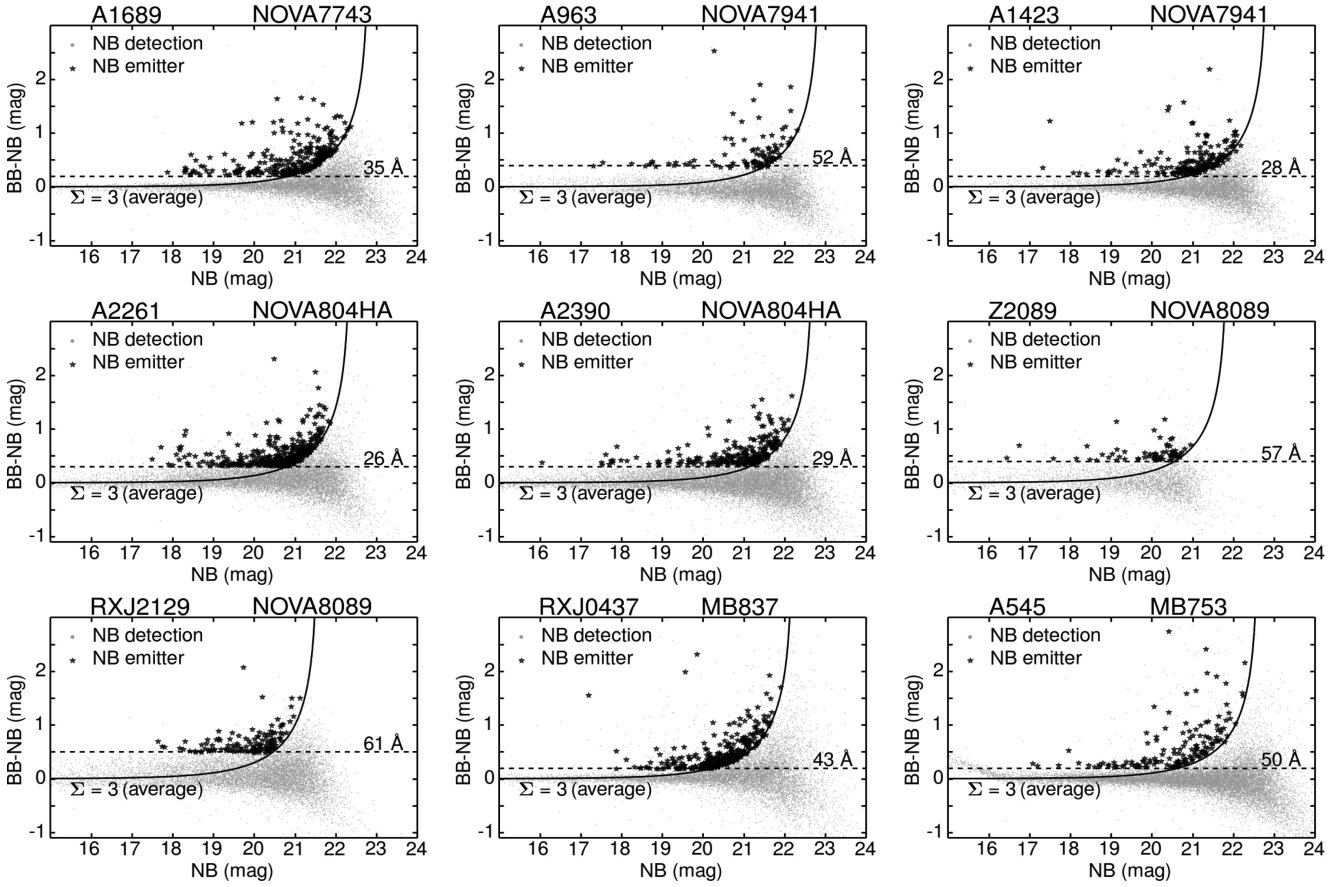

Figure 3. Colour–magnitude diagrams of the colour excess as function of NB magnitude. We select emitters separately on each CCD for each cluster and adapt the cuts to reflect the noise levels reached in each observation. The curve represents the average 3Σ colour significance and the dashed, black line represents the rest-frame EW_0 cut.

We remove bad frames that are affected by bad weather (bad seeing, clouds, Saharan dust) and technical issues (loss of guiding, read-out issues). We also removed twilight flats which had too low or too high counts, thus being outside of the linearity range for the cameras. We median combine biases for each night to obtain a 'master' bias. We subtract the overscan from the science and twilight flat frames using the 'master' bias. We obtain a 'master' flat by median combining the twilight flats for each filter and renormalizing to 1. We correct the science frames by dividing through the 'master' flat.

In the red filters, our data suffer from 'fringing', thin film interference in the CCD coating. To correct for this, we detect sources in science exposures using SEXTRACTOR and subsequently mask them. We then median combine the masked science frames to obtain a 'super-flat'. We divide the data by the 'super-flat' to correct for 'fringing'.

Starting from an initial approximate astrometric solution, we use a few iterations of SCAMP to refine the solutions over the large FOVs of our cameras. Source positions were compared with positions in the bluest band of the 2MASS(Skrutskie et al. 2006). MISSFITS was used to update the header with the new astrometry in between SCAMP runs.

To bring the science exposures to the same scale, we derive zero-points (ZP) by comparing magnitudes of non-saturated objects with the closest band from the fourth United States Naval Observatory (USNO) CCD Astrograph Catalogue (UCAC4; Zacharias et al. 2013). The science frames with the same ZP are median combined and background subtracted to produce final images using SWARP.

We photometrically calibrate our data using the closest reference band in the SDSS Data Release 9 (SDSS DR9; Ahn et al. 2012), when available. Some of the cluster fields are not covered by SDSS, so we use the all-sky USNO-B1.0 catalogue (Monet et al. 2003). We follow the methods described in Stroe et al. (2014a) to calibrate USNO-B1.0 magnitudes against the SDSS DR9 scale. We then transfer the SDSS scale to our data, using the USNO-B1.0 magnitudes as reference. We perform the photometric ZP determination for each CCD separately.

We mask saturated sources and extract magnitudes in apertures of 5 arcsec in diameter using SEXTRACTOR in each CCD separately. This diameter was chosen to be large enough ($\sim$15 kpc) to encompass the bulk of the Hα emission at the redshifts ($0.15 < z < 0.31$) of our clusters. We correct all the magnitudes for Galactic dust extinction following the method described in Stroe et al. (2014a), using the Schlafly & Finkbeiner (2011) extinction values and interpolating to the effective wavelengths of our filters by using their model.

The average 3σ limiting magnitudes as well as the spread in the values between the different camera chips are reported in Table 4. The values presented are calculated after correcting for Galactic dust extinction, hence represent intrinsic depth values. Differences between the depth in each chip of the same camera are caused by variations in sensitivity and quality of the CCDs as well as the amount of Milky Way dust extinction.

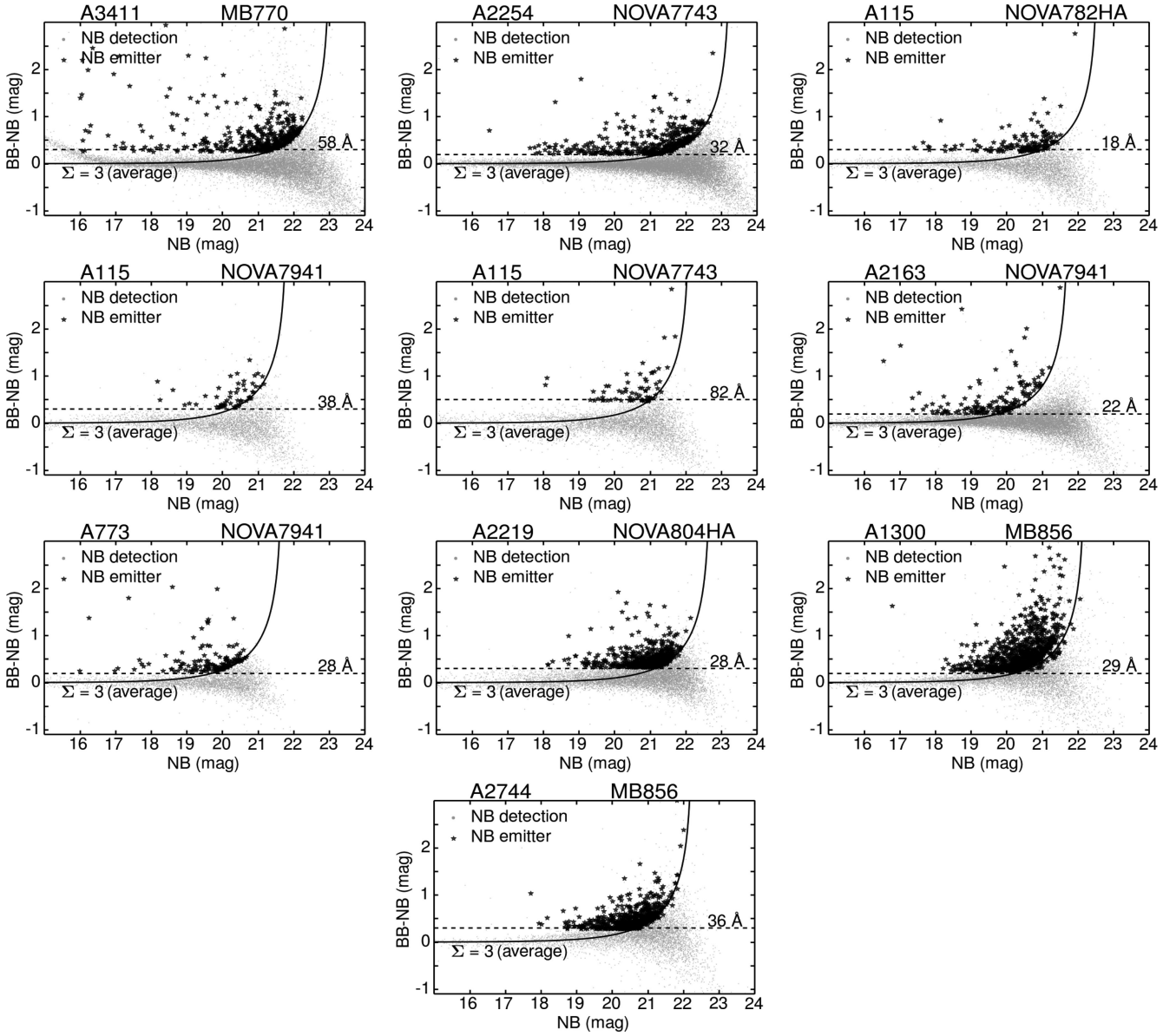

Figure 3 – *continued*

4 SELECTING Hα EMITTING SOURCES

We cross-match the BB subtraction filter data with the NB data. We combine this catalogue with the ancillary optical, IR and spectroscopic data in order to discriminate between different types of sources and to study them in greater detail.

4.1 Selection of NB excess sources

To identify emission line systems, we first need to select sources with excess emission in NB filter compared to the BB – this indicates the likely presence of an emission line located within the NB filter. We only select sources with a significant S/N (higher than 5). In practice, we apply these criteria using the formalism developed by Bunker et al. (1995), using a colour excess significance (Σ) and an equivalent width (EW) cut. The colour excess significance cut ensures we select only sources with real NB excess (compared to a random scatter of colour excess), while the EW cut ensures we select sources with line excess emission higher than the scatter of the excess at bright magnitudes.

Slight mismatches between the effective central wavelength of the NB filter compared to the BB can cause a systematic colour offset between magnitudes measured in the two filters. Therefore, we first correct for this effect by correcting for the median colour of sources with bright, non-saturated magnitudes. Fig. 3 shows the dependence of the excess BB–NB colour on the NB magnitude, together with the EW and Σ cuts used to select emitters.

Σ is then defined as (Sobral et al. 2013):

$$\Sigma = \frac{10^{-0.4(m_{\rm BB}-m_{\rm NB})}}{10^{-0.4({\rm ZP}_{\rm AB}-m_{\rm NB})}\sqrt{\pi r^2\left(\sigma^2_{\rm NB}+\sigma^2_{\rm BB}\right)}}, \quad (1)$$

where $m_{\rm NB}$ and $m_{\rm BB}$ are the NB and BB magnitudes, respectively, ${\rm ZP}_{\rm AB}$ is the magnitude system zero-point, r is the radius of the aperture used to extract the magnitudes measured in pixels (equivalent

to 5 arcsec in our case) and $\sigma_{\rm NB}$ and $\sigma_{\rm BB}$ are the rms noise levels in counts, as discussed towards the end of Section 3.3.

The flux density f is defined as:

$$f_{\rm NB,BB} = \frac{c}{\lambda^2_{\rm NB,BB}} 10^{-0.4(m_{\rm NB,BB} - {\rm ZP_{AB}})}, \quad (2)$$

where λ is the effective central wavelength of the NB and BB filters, respectively, and c is the speed of light. The line flux is calculated from the NB and BB fluxes in the following way:

$$F_{\rm line} = \Delta\lambda_{\rm NB} \frac{f_{\rm NB} - f_{\rm BB}}{1 - \Delta\lambda_{\rm NB}/\Delta\lambda_{\rm BB}}, \quad (3)$$

where $\Delta\lambda$ is the width of the NB and BB filters, respectively.

Finally, the EW is calculated as from the NB and BB fluxes:

$${\rm EW} = \Delta\lambda_{\rm NB} \frac{f_{\rm NB} - f_{\rm BB}}{f_{\rm BB} - f_{\rm NB}(\Delta\lambda_{\rm NB}/\Delta\lambda_{\rm BB})}. \quad (4)$$

The rest-frame ${\rm EW}_0$ at the redshift z of the object is:

$${\rm EW}_0 = {\rm EW}/(1+z). \quad (5)$$

We select as emitters the sources which fulfil the following criteria:

(i) $\Sigma > 3$: to ensure we select real sources.

(ii) EW larger than three times the scatter of the BB minus NB colour, in the non-saturated, high S/N regime, to ensure we select real excess sources. The exact cut depends on the cluster, because of the different depths reached in each field.

The number of emitters selected is listed in Table 4.

4.2 Identifying point sources

After selecting the emitters, we visually inspect sources to flag potential artefacts as well as any potential star contamination. The number of stars depends heavily on the field, as most clusters are located away from the Galactic plane. However, some clusters (e.g. A545, A2390, 'Sausage', 'Toothbrush') are located close to the Galactic plane and/or centre. Stars with various features in their spectra can contaminate the sample of emitters: in some cases the NB filter can pick up the peak continuum while the BB can have a lot of the absorption, thus mimicking an emission line.

In order to tag an object as a star/point-like object, it has to fulfil any of the following criteria:

(i) Classified as star based on spectroscopy: whenever we have a spectroscopically confirmed star we remove it.

(ii) Classified as star based on morphology: a star is classified as such if we tag it as a star in the visual inspection and it is also unresolved. In order to check that a source is unresolved we require the source to have a FWHM smaller than the average of the field and well as an ellipticity below 0.2 in both the NB and the BB filter.

(iii) Classified as a star because of its IR colours (see Fig. 4): we use the criteria defined in Sobral et al. (2012), to select red stars:

$$(g-r) > 2(J-Ks) + 1 \;\&\; (g-r) > 0.8 \;\&\; (J-Ks) > -0.7. \quad (6)$$

(iv) Classified as a blue star or quasar according to the criteria from Sobral et al. (2012):

$$(g-r) > 2(J-Ks) + 1 \quad \& \quad (g-r) < 0.8. \quad (7)$$

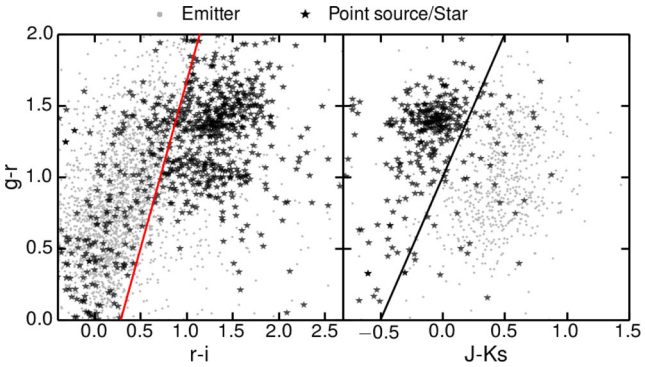

Figure 4. Colour–colour plots for emitters. The left plot displays the $g-r$ colour versus $r-i$. The right plot represents $g-r$ versus $J-Ks$. Point-like objects are represented with stars, while emitters are shown in grey dots. The lines show the colour cuts used to select point-like objects, in combination with other criteria as discussed in Section 4.2.

(v) Classified as a star because of its optical colours: we use the criteria defined in Stroe & Sobral (2015), which removes L and M dwarf stars:

$$(g-r) > (7/3(r-i) - 2/3) \quad \& \quad (g-r) > 1.0. \quad (8)$$

4.3 Selection of Hα candidates

The sample of potential line emitters is expected to be dominated by Hα emitters at the redshifts of the clusters. However, we will also detect other line emitters with shorter intrinsic wavelength, but redshifted at higher z compared to the cluster distance. The most numerous interlopers expected are: Hβ ($\lambda_{\rm rest} = 4861$ Å) and [O III] $\lambda\lambda$4959, 5007 emitters at $z \sim 0.52$–0.74 and [O II] ($\lambda_{\rm rest} = 3727$ Å) emitters at $z \sim 1.0$–1.3, and to a lesser degree 4000 Å break galaxies (e.g. Shioya et al. 2008; Stroe & Sobral 2015).

Fig. 5 lists the rest-frame wavelength of emitters for which we have a spectroscopic redshift. We also overplot the wavelength ranges where given a filter width of 200 Å (maximum width of the NB filters we use) would pick up these lines. The Hα selection is very good, as exemplified by the clear peak in around the Hα wavelength.

We classify emitters as high-confidence Hα, uncertain and definitely not Hα. We can outright remove an emitter if we have spectroscopy confirming it is an emitters at higher redshift (Fig. 5). We mark a source as high-confidence Hα if it fulfils at least one of these two criteria: (i) it has a size of more than 4 arcsec on the sky, (ii) its spectroscopic redshift is within the redshift range covered by the NB filter. The first criterion was used in Stroe et al. (2014a), as high-z emitters have a very low chance to reach sizes imposed by a 4 arcsec aperture (10–15 kpc size for the redshift range covered by our sources). If these sources were higher redshift, they would be at least 25 kpc if they were [O III] emitters at $z \sim 0.5$ and 34 kpc if they were [O II] emitters at $z \sim 1.3$. For many sources we have spectroscopy confirming their Hα nature, however this of course does not cover all the sources picked up by the NB filter. However, note the very prominent peak around the Hα wavelength for emitters with redshift, which indicates our selection is reliable for Hα sources (Fig. 5).

The rest of the sources can either be Hα or other line emitters. With the bands that we possess and the non-uniform data availability and quality for each cluster, it is hard to securely separate Hα emitters from other high-z emitters. On a case by case basis, for

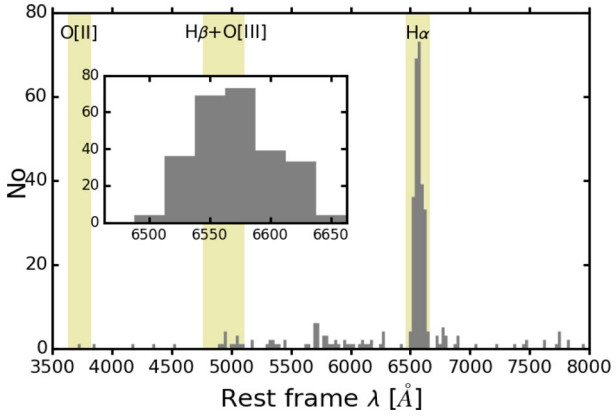

Figure 5. Histogram of the distribution of emitters with spectroscopic redshift. Because of the different NB filters tracing different redshift ranges, we transform into the rest frame of the main emission line. The ranges for which Hα, O[II], Hβ and O[III] emitters are expected to be picked up by our filters are marked with the shaded areas. The distribution is clearly dominated by Hα emitters indicating the filters properly select emitters. Note however, that most of the spectra were targeting the red sequence of the clusters, hence the number of emitters with spectra is rather low. However, the chance of an emitter at the cluster redshift to have a spectrum is still much larger than if they were at a higher redshift, hence there is a bias in source redshifts. The number of spectra for sources at different redshift from the cluster distance is therefore lower than in reality.

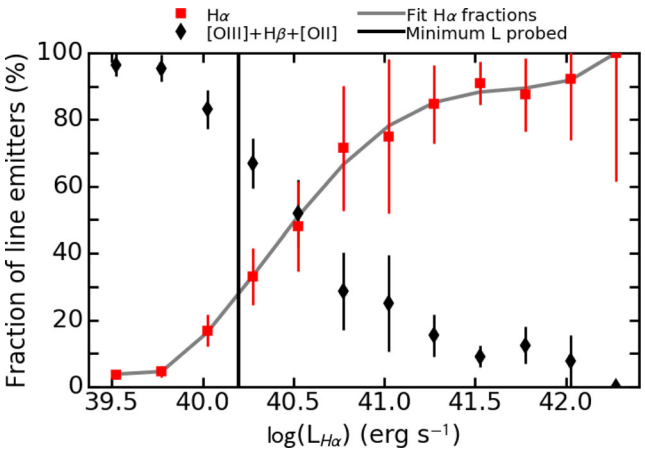

Figure 6. Fraction of Hα emitters expected from a population of line emitters selected with a NB survey, as function of Hα luminosity. The grey line displays the Hα fraction fit as a function of the luminosity.

smaller sources without spectroscopy, we cannot be sure they are Hα emitters or other high-z emitters. We therefore follow the statistical method of Stroe et al. (2014a) of using high-quality data in deep extragalactic fields to study the fraction of Hα emitters in a population of line emitters. We improve on the work from Stroe et al. (2014a) by adding new data from Stroe & Sobral (2015). We therefore combine three data sets: very deep COSMOS Hα NB data at $z \sim 0.4$ (Sobral et al. 2013) and at $z \sim 0.2$ (Shioya et al. 2008), with relatively poor coverage for bright sources, and wide area Hα data at $z \sim 0.2$ to especially have a better handle of the fractions for bright sources (Stroe & Sobral 2015). As expected, towards high fluxes (i.e. at bright luminosities) the Hα fraction increases fast, as shown in Fig. 6. The functional form for the Hα fraction dependence on the luminosity is shown below:

$$\begin{aligned} \mathrm{frac}_{\mathrm{H}\alpha} = {} & 13.448 \log^4\left(\frac{L_{\mathrm{H}\alpha}}{\mathrm{erg\,s^{-1}}}\right) - 2206.61 \log^3\left(\frac{L_{\mathrm{H}\alpha}}{\mathrm{erg\,s^{-1}}}\right) \\ & + 1.356 \times 10^5 \log^2\left(\frac{L_{\mathrm{H}\alpha}}{\mathrm{erg\,s^{-1}}}\right) - 3.708 \\ & \times 10^6 \log\left(\frac{L_{\mathrm{H}\alpha}}{\mathrm{erg\,s^{-1}}}\right) + 3.798 \times 10^7. \end{aligned} \quad (9)$$

When building an Hα LF (see Section 5.6), we apply the fractions derived above to statistically select the appropriate number of Hα sources, from the pool of emitters. The number of likely Hα emitters, including confident Hα sources as well as number of Hα obtained by applying the fractions for the rest of the emitters, are listed in Table 5. The number of emitters in each field can be found in Table 4. The total number of emitters is 5905.

5 Hα LUMINOSITY FUNCTION

The LF of Hα emitters is obtained by binning emitters depending on their luminosity, diving by the survey volume and fitting with a Schechter function (see Section 5.6, Schechter 1976) to described the density of emitters. With the goal of building LFs by combining different fields based on cluster properties, we first need to obtain Hα fluxes and correct for incompleteness arising from our EW and Σ cuts, as well as correct the probed cosmic volumes for the filter profile. These steps are described below.

5.1 [N II] contamination

Given the small difference in wavelength, our NB filters will measure the sum of Hα and $[\mathrm{N\,II}]_{6450,\,6585}$. Therefore, the line flux we measure needs to be corrected to obtain Hα fluxes. We remove the [N II] contamination from the flux using the relation derived by Sobral et al. (2012), in which the [N II] contamination to the flux is a function of EW:

$$\begin{aligned} f = {} & -0.924 + 4.802E - 8.892E^2 + 6.701E^3 \\ & - 2.27E^4 + 0.279E^5, \end{aligned} \quad (10)$$

where f is the log of the ratio of [N II] to the total flux and $E = \log_{10}(\mathrm{EW}_0(\mathrm{H}\alpha + [\mathrm{N\,II}]))$. The mean [N II] contamination is about 30 per cent of the total blended flux and is consistent with spectroscopy from e.g. Sobral et al. (2015). This corresponds to roughly sub-solar to solar metallicity sources.

5.2 Hα luminosity

After correcting for the [N II] contamination, we calculate corrected Hα fluxes $F_{\mathrm{H}\alpha}$. The Hα luminosity is then defined as:

$$L_{\mathrm{H}\alpha} = 4\pi D_L^2(z) F_{\mathrm{H}\alpha}, \quad (11)$$

where $D_L(z)$ is the luminosity distance of each cluster (see Table 2).

5.3 Completeness correction

At faint luminosities or low EW, our survey will only recover a fraction of the true number of sources. We correct for incompleteness by selecting random subsamples of sources consistent with being non-emitters and adding increasing larger line fluxes to their fluxes. We then pass the fake emitters through the same selection criteria as the real sources (see Section 4). We perform the study independently for each sources and each individual CCD to test how many

sources we recovered as function of luminosity. At each luminosity, we correct the LF for incompleteness. We refer the readers to Sobral et al. (2012) and Sobral et al. (2013) for further details on the method.

5.4 Filter correction

Table 2 lists the expected cosmic volumes probed in each field, taking into account the effective area covered by the camera on sky, after masking bright stars and noisy regions. The volumes vary with the FWHM of the NB filters as well as the redshift of Hα we are tracing in each field. The volumes are initially calculated assuming the NB filters have a perfect top-hat (TH) shape with a FWHM as stated in Table 3. However, the actual shape of the filters deviates from a TH (see Fig. 2), which means not all sources located in the wings of the filter will be detected. Following the method described in Sobral et al. (2009) and Sobral et al. (2012), we correct the LF for the shape of the filters to take into account the sources missed at the edge of the filter. For each field and filter, we generate a sample of Hα emitters as would be selected by a perfect TH filter and bin them according to luminosity. We compute a first pass LF fit by a Schechter function. We then generate an idealized sample of Hα emitters according to the Schechter function just derived. We then pass this idealized population through the real filter profile to study the recovery rate of emitters at each wavelength covered by the filter.

5.5 Survey limits

At 50 per cent completeness, the average limiting Hα luminosity varies between $10^{40.2}$ and $10^{41.3}$ erg s^{-1} (for full details see Table 4). This is driven by the depth of the observations as well as the redshift of the sources. Assuming the Kennicutt (1998) relation, corrected for a Chabrier IMF, this corresponds to limiting SFRs of 0.07–0.78 M$_\odot$ yr^{-1}, when no intrinsic dust extinction is applied. This corresponds to 0.03–0.3 SFR* at the respective redshifts of the clusters, with the average being 0.1 SFR*.

5.6 Hα luminosity function

We bin the emitters based on luminosity, corrected for [N II] contamination, and add their associated inverse volume to obtain LFs. We only add sources in volumes with at least 50 per cent completeness. As mentioned in Section 4.3, we count the sources we are confident are Hα emitters with a weight of 1 and we apply a statistical Hα probability fraction for sources we cannot be sure are Hα and not higher z sources. We correct the LFs for incompleteness and for the filter profile, but note that we are not correcting for intrinsic dust extinction.

We use a least-squares fit to parametrize the binned data with a Schechter (1976) function, using Poissonian errors:

$$\phi(L_{\rm H\alpha}){\rm d}L_{\rm H\alpha} = \phi^* \left(\frac{L_{\rm H\alpha}}{L^*_{\rm H\alpha}}\right)^{\alpha} {\rm e}^{-\frac{L_{\rm H\alpha}}{L^*_{\rm H\alpha}}} {\rm d}\left(\frac{L_{\rm H\alpha}}{L^*_{\rm H\alpha}}\right), \quad (12)$$

where ϕ^* is the typical number density of Hα sources, $L^*_{\rm H\alpha}$ is the characteristic luminosity and α is the faint-end slope of the LF. We allow for all three parameters of the fit to vary freely. We perform the fit using a range of different log L bins: with widths $\Delta\log L$ from 0.15 to 0.4 and starting bins log $L_{\rm min}$ ranging from 40 up to 40.5.

We tested a number of different ways to bin the data in order to avoid reporting parameters which could be biased by a particular binning choice. We first binned the data with a random choice of bin widths and bin centres and fit a LF to all the resampled data. Secondly, we also rebinned these resamples to a wider L grid and fit an average LF. We also fit individual LFs to each of our random choices of bin width and calculated the average of the results.

We also tested fits with all three parameters free and found that in many cases the overall fit was biased because of the faint-end slope. To test the robustness of the fits with α, ϕ^* and L^* free, we studied the faint end by fitting a straight line to only the faintest bins and found that in some cases this did not match the α obtained by fitting a full LF to all the data.

In order to further test this, we also performed a resampling analysis, where for each combined volume, we removed one-by-one each cluster from the stack, to see whether a particular cluster is dominating the fit. We discovered that the fits were not robust when removing a cluster from the fits, and the LF fits to these data, while consistent within the error bars, were in many cases at the very edge of inconsistency to the LF obtained using all the clusters in the 'stack'. Additionally the error bars on each LF parameter were large. We conclude that we cannot derive a very robust faint-end slope value. This is mostly driven by the depth of our data. Additionally, when combining different clusters, at the very faintest bins, the combined LF is dominated by a few clusters, which might bias the results. We therefore decided to fit LFs by fixing α to values derived from deep data, specifically -1.35 from Shioya et al. (2008) and -1.7 from Ly et al. (2007). We find that our LF parameters have lower errors and are more robust against removing individual clusters from the combined volume when using the flatter faint-end slope -1.35.

We also noticed that at the very brightest luminosities, beyond $10^{42.2}$ erg s^{-1}, there was a very high bin, inconsistent with the usual drop of the LF towards these luminosities. This is caused by <5 sources above the expected Poissonian variation. Even though these have passed visual inspection, they are compact sources and hence they could be AGN. We will follow up these sources and inspect their nature in a future paper. For this study, in order to make out fits more robust, we are not considering bins with $L > 42.2$ in our LF fits.

Overall, after fixing the faint end and removing the very bright luminosity bins, we find that all the methods we used to bin the data and fit LFs produce results which are consistent within the error bars. In general, the individual binning choices also agree with the average fits within the errors, with the exception of a limited number of binning choices, as expected. We finally bin all the ϕ values obtained with a range of bin widths and bin centres to produce an average binning. We calculate the error as the standard deviation of the *phi* values falling within each final bin. We therefore report the LF parameters resulting from a binning which reproduced well the average LF and also results in LF parameters with small errors, again indicating a good fit.

6 RESULTS

Our main goal for this work is to contribute to our understanding of the drivers of SF in clusters. In order to do so, we need to compare relaxed and merging clusters, look for any trends with mass and/or luminosity and of course compare to results obtained over wide areas to quantify the statistical behaviour of the Universe in lower density environments. Therefore, we bin the emitters based on a number of criteria, according to the cluster properties listed in Table 1.

Table 5. Parameters of LFs for different Hα samples, with faint-end slope $\alpha = -1.35$. These were selected inside and outside the clusters, and in clusters of different relaxation states, masses, luminosities and redshifts. We also list the total volume of each of the combined LFs. The last column lists the number of likely Hα emitters, including secure Hα emitters confirmed through spectroscopy or their size. For the rest of the emitters we applied the fractions derived in equation (9).

Stack	$\log \phi^*$ (Mpc^{-3})	$\log L^*_{\mathrm{H}\alpha}$ (erg s^{-1})	V (10^4 Mpc^3)	Hα sources
Stroe & Sobral (2015) fit	-2.85 ± 0.03	41.71 ± 0.02	–	–
All cluster fields	$-1.95^{+0.06}_{-0.06}$	$41.56^{+0.05}_{-0.05}$	13.0	3472
Inside 2 Mpc	$-1.98^{+0.06}_{-0.04}$	$41.56^{+0.03}_{-0.03}$	4.4	1203
Beyond 2 Mpc	$-1.92^{+0.04}_{-0.06}$	$41.53^{+0.05}_{-0.05}$	8.6	2211
Merging, 0–0.5 Mpc	$-1.59^{+0.06}_{-0.07}$	$41.68^{+0.09}_{-0.06}$	0.2	92
Relaxed, 0–0.5 Mpc	$-1.92^{+0.07}_{-0.11}$	$41.71^{+0.09}_{-0.06}$	0.1	49
Merging, 0.5–1.0 Mpc	$-1.71^{+0.06}_{-0.04}$	$41.56^{+0.03}_{-0.03}$	0.4	174
Relaxed, 0.5–1.0 Mpc	$-2.04^{+0.03}_{-0.05}$	$41.50^{+0.01}_{-0.01}$	0.5	94
Merging, 1.0–1.5 Mpc	$-1.77^{+0.06}_{-0.06}$	$41.56^{+0.05}_{-0.03}$	6.0	248
Relaxed, 1.0–1.5 Mpc	$-2.31^{+0.06}_{-0.09}$	$41.62^{+0.09}_{-0.05}$	6.8	107
Merging, 1.5–2.0 Mpc	$-1.92^{+0.09}_{-0.09}$	$41.50^{+0.08}_{-0.06}$	8.0	241
Relaxed, 2.0–2.0 Mpc	$-2.28^{+0.04}_{-0.06}$	$41.71^{+0.08}_{-0.06}$	8.9	159
Merging, outside 2.0 Mpc	$-1.86^{+0.05}_{-0.04}$	$41.53^{+0.05}_{-0.03}$	46.6	1574
Relaxed, outside 2.0 Mpc	$-2.13^{+0.04}_{-0.05}$	$41.53^{+0.06}_{-0.06}$	33.3	599
Mergers	$-1.80^{+0.06}_{-0.07}$	$41.53^{+0.05}_{-0.03}$	1.9	755
Relaxed	$-2.16^{+0.06}_{-0.06}$	$41.59^{+0.05}_{-0.05}$	2.1	409
Relics	$-1.53^{+0.06}_{-0.09}$	$41.41^{+0.03}_{-0.01}$	1.0	430
Haloes or haloes and relics	$-1.80^{+0.05}_{-0.06}$	$41.53^{+0.03}_{-0.01}$	1.6	632
Low z ($0.15 < z < 0.20$)	$-1.98^{+0.06}_{-0.06}$	$41.59^{+0.06}_{-0.03}$	0.8	292
Mid z ($0.20 < z < 0.25$)	$-2.28^{+0.04}_{-0.08}$	$41.65^{+0.07}_{-0.05}$	2.9	574
High z ($0.25 < z < 0.31$)	$-1.17^{+0.04}_{-0.06}$	$41.32^{+0.03}_{-0.01}$	0.7	337
Low mass[b] ($4 \times 10^{14}\,\mathrm{M}_\odot < M < 10 \times 10^{14}\,\mathrm{M}_\odot$)	$-2.58^{+0.09}_{-0.10}$	$41.86^{+0.15}_{-0.08}$	2.1	388
High mass ($10 \times 10^{14}\,\mathrm{M}_\odot < M < 29 \times 10^{14}\,\mathrm{M}_\odot$)	$-1.89^{+0.04}_{-0.03}$	$41.53^{+0.03}_{-0.03}$	2.0	776
Low L (5×10^{44} erg s^{-1} $< L_{\mathrm{X}} < 10 \times 10^{44}$ erg s^{-1})	$-2.22^{+0.11}_{-0.12}$	$41.68^{+0.19}_{-0.10}$	2.1	425
High L (10×10^{44} erg s^{-1} $< L_{\mathrm{X}} < 38 \times 10^{44}$ erg s^{-1})	$-1.77^{+0.04}_{-0.05}$	$41.50^{+0.03}_{-0.03}$	1.8	755

[a]Faint-end slope was fixed to value derived in Shioya et al. (2008).
[b]A1300 was removed from the stack as it was dominating the LF fit.

(i) General, all fields sample: we bin all the emitters for all the fields, both inside and outside of the clusters.
(ii) Environment:

(a) Clusters: we stack all the emitters within clusters out to a projected radius of 2 Mpc away from the cluster centre.
(b) Field around clusters: stack of emitters located around the cluster, more than 2 Mpc away from the cluster centre.

(iii) Merger state:

(a) Relaxed clusters: stack of all the relaxed clusters.
(b) Merging clusters: clusters that host relics and clusters that host haloes.

(iv) Mass of the cluster – bin emitters within clusters of certain mass (low and high mass).
(v) Luminosity – bin cluster emitters depending on the host cluster X-ray luminosity (low and high X-ray luminosity).

This information is also summarized in Table 5, where we also list the best-fitting Schechter function parameters, volumes of each combined data set and the number of Hα emitters used to produce the LFs. As reference for these LFs, we use the $z \sim 0.2$ Hα LF derived in Stroe & Sobral (2015), which combines deep data within a smaller FOV (Shioya et al. 2008) to capture faint Hα emitters, with shallower data over a large field to overcome cosmic variance and capture rare, bright emitters. Our survey sits at a third of the volume from Stroe & Sobral (2015) ($\sim 1.3 \times 10^5$ Mpc^3 compared to the larger 3.5×10^5 Mpc^3), albeit our Hα emitters are selected over a wider redshift spread. A typical deep field NB Hα survey such as the one of Shioya et al. (2008) covers $\sim 3.1 \times 10^4$ Mpc^3. Most of our combined data sets reach volumes of 50–75 per cent of that value. The smallest volumes are for the combined cluster cores, as well as for the low-z data, as expected. The small volumes will of course mean our combined volumes are highly sensitive to cosmic variance, as is already exemplified by the differences in the numbers of Hα emitters in each combined data set. For example, for similar volumes, the mergers combined data set has a factor of ~ 1.8 more Hα sources than the relaxed cluster data. However this enables us to investigate environmental trends.

6.1 Environment

Compared to the large Hα survey from Stroe & Sobral (2015) which covers voids, rich and dense fields and greatly overcomes cosmic

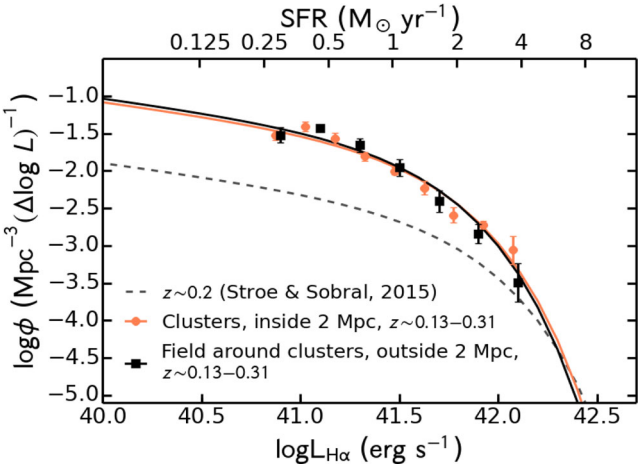

Figure 7. The Hα LF averaged over all the clusters in our sample, within 2 Mpc of the cluster centre. The cluster LF is consistent with the larger scale environment of the clusters beyond 2 Mpc. However, compared to an average field (Stroe & Sobral 2015), the clusters reside in overdense environments. Note that the Hα properties inside and outside of the clusters are very different for merging and relaxed clusters (see Fig. 8).

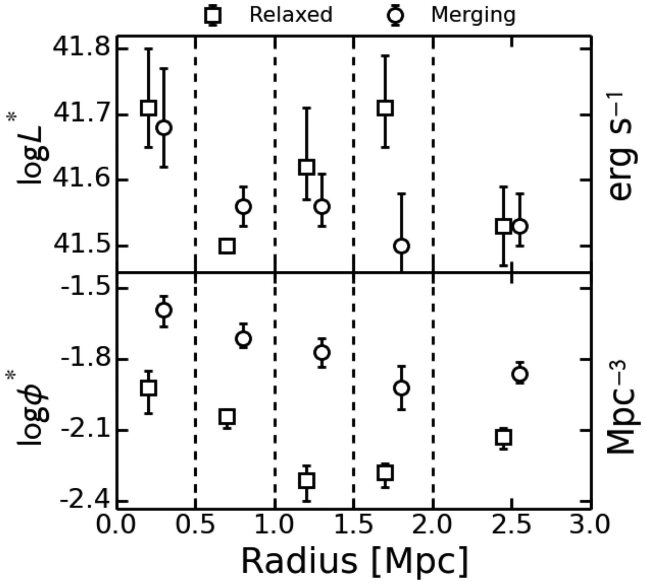

Figure 8. Dependence of the Hα LF parameters on environment. Points have been shifted in projected radius for clarity. There are striking differences between the behaviour of relaxed and merging clusters in both ϕ^* and L^*. The emitters are binned in five regions, indicated with the vertical dashed lines: a circle within 0.5 Mpc from the centres of each cluster, an annulus between 0.5 and 1 Mpc radius, another annulus between 1 and 2 Mpc and then all emitters outside of 2 Mpc from the cluster centre.

variance, we find that, statistically, the cluster fields targeted in this survey live in generally rare/extreme, overdense environments (at $>27\sigma$ level). Otherwise, the characteristic luminosity is in agreement (difference of less than 3σ). This is interesting since Stroe & Sobral (2015) used both very deep data over a small field as well as a very large, shallow survey to obtain the LF. Stroe & Sobral (2015) predict that from cosmic variance, our ϕ^* and L^* of sources should be within 25–30 per cent from numbers obtained in a very large survey. Our survey is right at the edge of this prediction, which is expected given the survey is targeting the densest parts of the Universe.

On average, the LF in the cluster sample (within a projected radius of 2 Mpc of the cluster centre) is similar to that in the field around them (outside 2 Mpc from the cluster centre). This is illustrated in Fig. 7. However, this average shape is obtained by averaging between the opposing behaviours of the relaxed and merging clusters.

However, when dividing in smaller annular regions, we find trends with cluster-centric projected radius (see Fig. 8). The dependence with radius of the LF parameters differs between relaxed and merging clusters. While both have similar L^* values at the core and outside the clusters, the trends between 0.5 and 2.0 Mpc are vastly different. While for relaxed clusters the characteristic luminosity slowly rises across this region, for merging clusters it systematically drops from the cluster core to the value in the field outside the cluster (beyond 2 Mpc from the cluster centre). In terms of characteristic density, there is a trend of dropping ϕ^* from cores to outskirts (1.5–2 Mpc). However, for the relaxed clusters ϕ drops below the field value for the cluster outskirts, for the merging cluster no regions falls below the field around the clusters. Overall, every region within merging clusters is denser in Hα emitters when compared to the densest region (the core) of relaxed clusters.

6.2 Relaxation state

Merging environments are different from relaxed clusters: merging clusters have a higher ϕ^* (at 4σ level) and are overdense in Hα emitters at all luminosities, compared to relaxed cluster fields (see left-hand panel of Fig. 9). As mentioned before, the merging clusters are on average more massive than the relaxed cluster, however the different average cluster mass of the merging and relaxed samples cannot explain the differences we see, as will also be shown in Section 6.4.

6.3 Presence of shocks and turbulence

Clusters hosting shocks, have on average, higher characteristic Hα densities and lower L^* compared to those hosting turbulence, marked by the presence of radio haloes (see right-hand panel of Fig. 9). The differences are significant at the ∼3–4σ level.

There seems to be evidence for a decreasing L^* and increasing ϕ^* from relaxed, to halo-hosting clusters to relic hosting clusters. This indicates that relic clusters host numerous Hα emitters fainter than the characteristic luminosity. By contrast, high luminosity emission might be suppressed.

6.4 Cluster mass and X-ray luminosity dependence

An important aspect is that the high-L combined volume contains both relaxed and merging objects in equal numbers (four relaxed and four merging for the high-L 'stack'). However, the high mass combined volumes are dominated by disturbed objects (eight merging versus three relaxed), so, with our sample, we cannot fully disentangle the effects of mass and relaxation state.

High X-ray luminosity clusters are overdense in Hα emitters compared to low-L clusters (see right-hand panel of Fig. 10). The differences between ϕ^* are $>3\sigma$ away. The L^* for the two samples are consistent within the error bars.

In the case of low- and high-mass clusters, we observed no significant differences in the shape of the LF. However, once we remove cluster A1300, which has a low mass, there are statistically significant difference between the low- and high-mass stacks in both the ϕ^* and the L^* (left-hand panel, Fig. 10). The low-mass combined

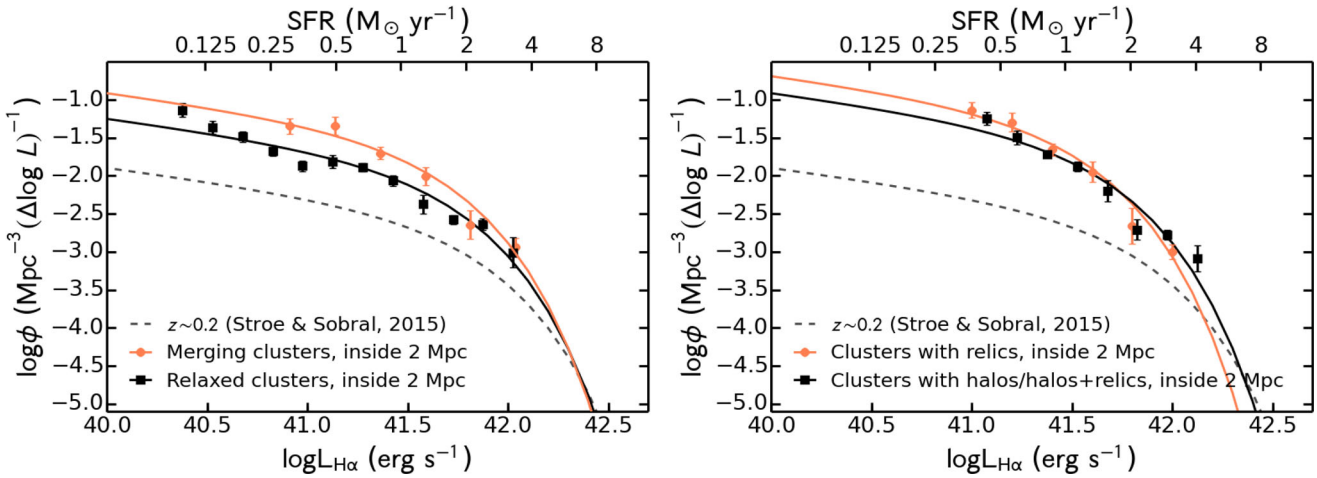

Figure 9. Left-hand panel: the Hα LF for merging and relaxed clusters (within 2 Mpc of centre). Note the differences in normalization of the two LFs. Right-hand panel: the Hα LF for clusters hosting relics and haloes, respectively (within 2 Mpc of centre). The presence of shocks mildly boosts the number of Hα emitters compared to a cluster hosting a halo.

volume is the only case where we find a single cluster to dominate the fit. We also note that the average mass of the high-mass combined volume is higher than the average mass of the merging cluster stack ($18 \times 10^{14}\,M_\odot$ versus $16 \times 10^{14}\,M_\odot$). However, the ϕ^* of the merging cluster stack is higher than that of the high-mass stack, indicating mass alone cannot explain the increased characteristic density of Hα emitters.

7 DISCUSSION

Relaxed clusters have a high density of galaxies compared to the fields around them. In stark contrast to field environments, passive galaxies represent a large fraction of the cluster population. Galaxies in $z = 0$ relaxed clusters are thought to have formed most of their stars in a single burst of SF at large cosmic time and then evolved passively without the possibility of accretion of new material. The hot ICM of relaxed clusters also has a profound influence on the fate of infalling galaxies: ram pressure stripping and other interactions may lead to the removal of gas, thus accelerating the evolution of field spirals into passive cluster ellipticals or S0s.

However, disturbed clusters have not been explored as much and they offer tantalizing opportunities to study environments and effects quite similar to high-redshift protoclusters. To test whether the SF properties of merging cluster galaxies are different from those in relaxed clusters, we are exploring our sample of ~20 clusters which span a range in mass, luminosity and redshift. Our goal is to find the main driver of SF and transformation of gas-rich spirals into gas-poor ellipticals in disturbed environments and their larger scale surroundings.

We find that both relaxed and merging clusters and their larger scale structure are overdense in Hα emitters when compared to an average cosmic volume. One might expect that the very low fraction of spiral galaxies in clusters would lead to a lower Hα LF normalization compared to an average field volume. Nevertheless, this seems not to be the case most probably because of the large overdensities of galaxies clusters represent. Clusters reside in a large web of filaments, which have been found to be rich in star-forming galaxies (Darvish et al. 2014). Our results support this scenario.

We also study the differences between relaxed and merging clusters, also separating into disturbed clusters hosting shocks (using relics as proxy) and those hosting increased turbulence (using haloes as proxy). The Hα properties of galaxies within relaxed and merging clusters are different. The ϕ^* and L^* vary in different ways with cluster centric distance for the two classes of clusters.

In the cores of both relaxed and merging clusters there seems to be a peak in characteristic luminosity and density. Important transformations can happen in the densest parts of the ICM: at cluster cores we could be seeing an increase in AGN activity and in galaxy–galaxy mergers.

For relaxed clusters, the characteristic densities of Hα emitters drop from core to immediate outskirts, where they fall below the field value around the clusters. This might indicate a suppression of SF in a fraction of infalling galaxies. However, the L^* of galaxies located towards relaxed cluster outskirts is higher than the field, indicating that in the galaxies surviving the infall into the cluster, there might be triggered SF. This could be caused for example by ram pressure stripping.

Merging clusters have a high ϕ^*, throughout the cluster volume, at all radii, staying always above the field levels. Therefore, merging clusters clearly present a very different environment from relaxed clusters. In disturbed clusters, the characteristic Hα number density is at least as high as the fields. The origin of these galaxies could either be recently accreted field spirals or triggering via ram pressure processes of infalling galaxies, however, we do not find any particular enhancement at the cluster outskirts. Dressler & Gunn (1983) found starbursting signatures in spectra of intermediate-redshift cluster galaxies, which they interpreted as 'ram pressure induced SF': the galaxies were shocked into an increased SFR, before the truncation of SF occurs. This scenario was later confirmed through simulations by Bekki & Couch (2003).

However, the enhancement in terms of numbers of Hα emitters prevails towards the 'cores' of disturbed clusters. Note that part of the emitters may be located towards the outskirts of the clusters, but seen in projection, however this cannot fully explain the increase in Hα number density towards the cluster centre. The general picture of massive galaxy clusters involves galaxy cluster populations undergoing a single massive burst of SF at high look back times (e.g. Eggen, Lynden-Bell & Sandage 1962; Partridge & Peebles 1967; Stevens et al. 2003; Rettura et al. 2010). Clusters would then grow by mergers with other relaxed clusters hosting predominantly passive galaxies, and by accretion of smaller, more disturbed clusters

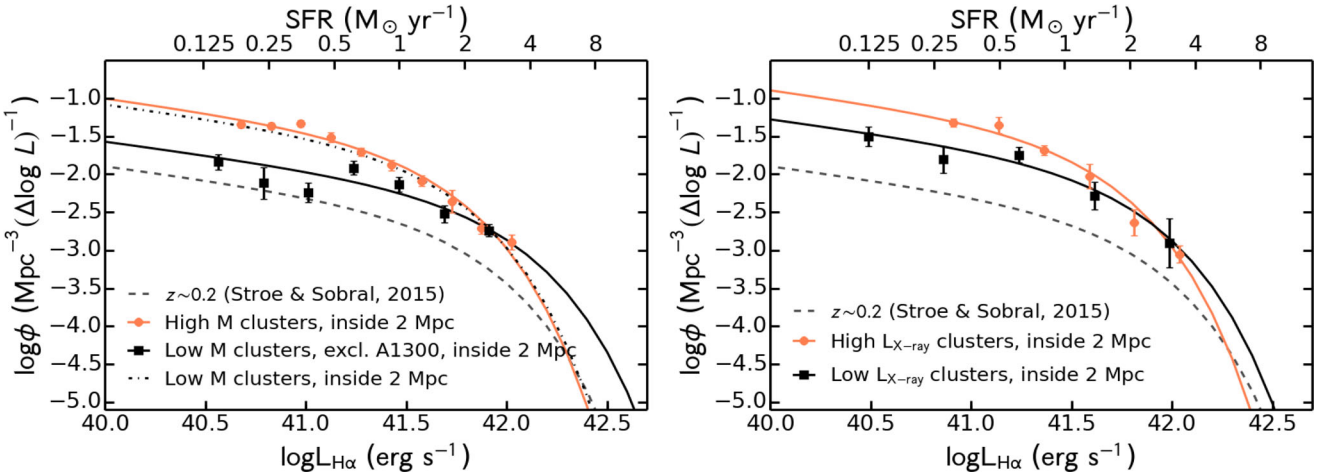

Figure 10. The Hα LF for stacks of low- and high-mass cluster (left-hand panel) and low- and high-luminosity clusters, respectively (right-hand panel). Only the emitters within 2 Mpc of the cluster centre were considered. There is marginal evidence for X-ray bright clusters hosting more numerous, lower luminosity Hα emitters on average. There are no differences between the low- and high-mass cluster LF, when A1300 is included in the low-M 'stack'.

hosting a larger fraction of spirals as well as field galaxies. The presence of active, Hα emitters deep in the core of disturbed clusters in our sample could indicate that the progenitors of the mergers were not relaxed, hence environmental quenching has not been operating for significant amounts of time. However this scenario fails to explain how the merging clusters we are studying have grown to be so massive, if the progenitors were also of young age, hence did not have a lot of time to grow their mass.

Another scenario would be that the merger induced processes which acted as a catalyst for SF. Roediger et al. (2014) adapted the ideas from Dressler & Gunn (1983) and Bekki & Couch (2003) into simulations where not necessarily ram pressure, but large-scale, low Mach number cluster shocks would traverse gas-rich galaxies. They found that indeed such shocks would be capable of triggering SF in cluster galaxies. This could be similar to cold gas streams proposed to fuel the growth of galaxies by penetrating shock-heated media of massive dark matter haloes (Dekel et al. 2009). Additionally these massive clusters could have accreted smaller, young subgroups as well as collapsed filaments which in combination with triggered SF could explain the increased Hα density.

Our results also indicate that merging clusters hosting haloes are closer in terms of SF properties to relaxed clusters than relic clusters (ϕ^* drops from relic, to halo cluster to relaxed clusters). This could indicate that either halo-hosting clusters are more dynamically evolved than relic clusters, which would allow the galaxies to further evolve into passive galaxies, explaining the deficit of mid-L Hα emitters. This is line with theory of diffuse radio emission, which indicates that the halo effect appears later than relics and is a more long lasting one (Brunetti & Jones 2014). Additionally, turbulence, if indeed correlated with haloes, might not have as much of an effect on SF as shocks. The large scale flows cascade into small-scale turbulence on scales of 10–100 kpc, thought to cause particle acceleration and hence radio haloes. A possibility is that the turbulence does not penetrate into the intragalactic medium and thus is not able to change galaxies' SF properties.

We find that cluster X-ray luminosity correlates more strongly with SF properties rather than cluster mass. Cluster mass cannot solely explain the evolution with relaxation state in the shape of the Hα LF. Naively, we would expect that massive clusters host a larger number of galaxies and assuming a fixed fraction of SF galaxies, hence a larger number of Hα emitters. However, cluster mass does not correlate well with cluster X-ray luminosity (Fig. 1), most probably because many of these clusters are not in hydrostatic equilibrium. Therefore, our results indicate the merger status of the host cluster plays an important role in setting the SF trends of cluster galaxies.

8 CONCLUSIONS

We performed an Hα narrow-band survey of a sample of 19 clusters with redshifts covering the 0.15–0.31 range. We selected >3000 likely Hα emitters over a total volume of $\sim 1.3 \times 10^5$ Mpc^3, located in a variety of environments. The Hα emitters are located in relaxed and merging clusters of low and high mass and luminosity, as well as in the large-scale environment of the clusters.

With our data, we are studying the effects of environment on the properties of the Hα LF, specifically focusing on the way disturbed clusters can drive the SF properties of their members. We also compare relaxed cluster environments to clusters with evidence for large shock waves and increased ICM turbulence. Our main results are:

(i) We build a first 'universal' Hα LF for clusters and their nearby environments. The LF is fit by a Schechter function with fixed $\alpha = -1.35$ and parameters $\log \phi^* = -1.95^{+0.06}_{-0.06}$ and $\log L^* = 41.56^{+0.05}_{-0.05}$. Cluster fields are overdense in Hα emitters compared to an average cosmic volume.

(ii) There is a significant difference between the properties of the Hα LF in relaxed and merging clusters, which cannot be solely attributed to the mass of the hosting clusters. The dependence of the LF parameters on cluster centric distance is different for merging and relaxed clusters.

(iii) At all projected cluster-centric radii, ϕ^* is much higher for merging clusters than for relaxed objects. Merging clusters, especially those with ICM shocks, have a density of Hα emitters slightly larger than the field around them.

(iv) For merging clusters, L^* drops slowly from cores to the field value just outside the cluster, while for relaxed clusters L^* increases towards cluster outskirts.

(v) We speculate that increased AGN activity and galaxy–galaxy mergers can elevate L^* and ϕ^* in the cluster cores. At the outskirts of relaxed clusters, accretion of gas-rich galaxies can lead to an

increase of the typical L^*. In merging clusters, triggered SF can occur through interactions with the ICM, cluster-wide shocks. The SF can also be increased through collapsed spiral-rich filaments and accretion of young galaxy groups.

(vi) X-ray luminosity, which is related to both mass and merger state of the cluster, seems to have a higher impact of the Hα LF than the mass alone. This corroborates the above results that the merger state of the host cluster has a high impact on the SF properties of cluster galaxies.

ACKNOWLEDGEMENTS

We thank the referee for the comments which improved the clarity of the paper. We are grateful to W. Dawson and N. Golovich for sharing their published data with us and H. Röttgering and D. Wittman for useful discussions. We thank B. Miranda Ocejo, S. Harish, S. Perez, J. Cairns, S. Dempsey and R. Kaiser for their help with the observations. DS acknowledges financial support from Lancaster University through an Early Career Internal Grant A100679, the Netherlands Organization for Scientific research (NWO), through a Veni fellowship, and from FCT through a FCT Investigator Starting Grant and Start-up Grant (IF/01154/2012/CP0189/CT0010). Based on observations made with the Isaac Newton Telescope (proposals I16AN002, I15AN001, I12BN003, I13BN006) operated on the island of La Palma by the Isaac Newton Group in the Spanish Observatorio del Roque de los Muchachos of the Instituto de Astrofísica de Canarias. The research leading to these results is part based on observations takes at the MPG 2.2m telescope, through the OPTICON programme (ID 14B039). OPTICON is supported by the European Community's Seventh Framework Programme (FP7/2013-2016) under grant agreement number 312430. We would like to thank M. Balogh, R. Barrena, W. Boschin, D. Coe, D. Frye, M. Girardi, R. Houghton, F. La Barbera, L. Lemonon, D. Lenze, M. Owers and M. Pierre for making their spectroscopic and photometric catalogues public. This study is based on observations obtained with MegaPrime/MegaCam, a joint project of CFHT and CEA/IRFU, at the Canada–France–Hawaii Telescope (CFHT), which is operated by the National Research Council (NRC) of Canada, the Institut National des Science de l'Univers of the Centre National de la Recherche Scientifique (CNRS) of France and the University of Hawaii. This work is based in part on data products produced at Terapix available at the Canadian Astronomy Data Centre as part of the Canada–France–Hawaii Telescope Legacy Survey, a collaborative project of NRC and CNRS. This study is partly based on observations obtained as part of the VISTA Hemisphere Survey, ESO Program, 179.A-2010 (PI: McMahon) and as part of the VST ATLAS survey, ESO Program, 177.A-3011 (Shanks et al. 2015). This paper makes use of data obtained from the Isaac Newton Group Archive which is maintained as part of the CASU Astronomical Data Centre at the Institute of Astronomy, Cambridge. This study is based on observations made with ESO Telescopes at the La Silla Paranal Observatory under programme ID 084.A-9001. We acknowledge Edward L. Wright and James Schombert for writing the cosmology calculator used throughout this paper. We have extensively used the NUMPY (van der Walt, Colbert & Varoquaux 2011), SCIPY (Jones et al. 2001), MATPLOTLIB (Hunter 2007) and ASTROPY (Astropy Collaboration et al. 2013) packages. This research made use of Montage, funded by the National Aeronautics and Space Administration's Earth Science Technology Office, Computational Technologies Project, under Cooperative Agreement Number NCC5-626 between NASA and the California Institute of Technology. The code is maintained by the NASA/IPAC Infrared Science Archive. This research has made use of the NASA/IPAC Extragalactic Database (NED) which is operated by the Jet Propulsion Laboratory, California Institute of Technology, under contract with the National Aeronautics and Space Administration. This research has made use of NASA's Astrophysics Data System. This research has made use of the VizieR catalogue access tool, CDS, Strasbourg, France. The original description of the VizieR service was published in Ochsenbein, Bauer & Marcout (2000). This research has made use of 'Aladin sky atlas developed at CDS, Strasbourg Observatory, France (Bonnarel et al. 2000; Boch & Fernique 2014).

REFERENCES

Abazajian K. N. et al., 2009, ApJS, 182, 543
Abraham R. G. et al., 1996, ApJ, 471, 694
Ahn C. P. et al., 2012, ApJS, 203, 21
Akamatsu H., Kawahara H., 2013, PASJ, 65,
Astropy Collaboration et al., 2013, A&A, 558, A33
Baade D. et al., 1999, The Messenger, 95, 15
Bacchi M., Feretti L., Giovannini G., Govoni F., 2003, A&A, 400, 465
Balogh M. L., Morris S. L., Yee H. K. C., Carlberg R. G., Ellingson E., 1999, ApJ, 527, 54
Balogh M. L., Couch W. J., Smail I., Bower R. G., Glazebrook K., 2002, MNRAS, 335, 10
Balogh M. et al., 2004, MNRAS, 348, 1355
Barrena R., Boschin W., Girardi M., Spolaor M., 2007a, A&A, 467, 37
Barrena R., Boschin W., Girardi M., Spolaor M., 2007b, A&A, 469, 861
Barrena R., Girardi M., Boschin W., de Grandi S., Eckert D., Rossetti M., 2011, A&A, 529, A128
Beck A. M., Dolag K., Donnert J. M. F., 2016, MNRAS, 458, 2080
Bekki K., Couch W. J., 2003, ApJ, 596, L13
Bertin E., 2006, in Gabriel C., Arviset C., Ponz D., Solano E., eds, ASP Conf. Ser., Vol. 351, Astronomical Data Analysis Software and Systems XV. Astron. Soc. Pac., San Francisco, p. 112
Bertin E., Arnouts S., 1996, A&AS, 117, 393
Bertin E., Mellier Y., Radovich M., Missonnier G., Didelon P., Morin B., 2002, in Bohlender D. A., Durand D., Handley T. H., eds, ASP Conf. Ser., Vol. 281, Astronomical Data Analysis Software and Systems XI. Astron. Soc. Pac., San Francisco, p. 228
Boch T., Fernique P., 2014, in Manset N., Forshay P., eds, ASP Conf. Ser., Vol. 485, Astronomical Data Analysis Software and Systems XXIII. Astron. Soc. Pac., San Francisco, p. 277
Böhringer H. et al., 2004, A&A, 425, 367
Böhringer H. et al., 2007, A&A, 469, 363
Bonnarel F. et al., 2000, A&A, 143, 33
Boschin W., Girardi M., Barrena R., Biviano A., Feretti L., Ramella M., 2004, A&A, 416, 839
Botteon A., Gastaldello F., Brunetti G., Dallacasa D., 2016, MNRAS, 460, L84
Brüggen M., van Weeren R. J., Röttgering H. J. A., 2012, MNRAS, 425, L76
Brunetti G., Jones T. W., 2014, Int. J. Mod. Phys. D, 23, 1430007-98
Bunker A. J., Warren S. J., Hewett P. C., Clements D. L., 1995, MNRAS, 273, 513
Butcher H., Oemler A., Jr1978a, ApJ, 219, 18
Butcher H., Oemler A., Jr1978b, ApJ, 226, 559
Canning R. E. A. et al., 2015, MNRAS, preprint (arXiv:1505.05790)
Chabrier G., 2003, PASP, 115, 763
Chung S. M., Eisenhardt P. R., Gonzalez A. H., Stanford S. A., Brodwin M., Stern D., Jarrett T., 2011, ApJ, 743, 34
Coe D., Benítez N., Broadhurst T., Moustakas L. A., 2010, ApJ, 723, 1678
Coe D. et al., 2012, ApJ, 757, 22
Cohen S. A., Hickox R. C., Wegner G. A., Einasto M., Vennik J., 2014, ApJ, 783, 136
Colless M. et al., 2001, MNRAS, 328, 1039

Dahle H., 2006, ApJ, 653, 954
Darvish B., Sobral D., Mobasher B., Scoville N. Z., Best P., Sales L. V., Smail I., 2014, ApJ, 796, 51
Darvish B., Mobasher B., Sobral D., Hemmati S., Nayyeri H., Shivaei I., 2015, ApJ, 814, 84
Darvish B., Mobasher B., Sobral D., Rettura A., Scoville N., Faisst A., Capak P., 2016, ApJ, 825, 113
Dawson W. A. et al., 2015, ApJ, 805, 143
Dekel A. et al., 2009, Nature, 457, 451
Donnert J., Dolag K., Brunetti G., Cassano R., 2013, MNRAS, 429, 3564
Donnert J. M. F., Stroe A., Brunetti G., Hoang D., Roettgering H., 2016, MNRAS, 462, 2014
Dressler A., 1980a, ApJS, 42, 565
Dressler A., 1980b, ApJ, 236, 351
Dressler A., Gunn J. E., 1983, ApJ, 270, 7
Dressler A. et al., 1997, ApJ, 490, 577
Driver S. P., Phillipps S., Davies J. I., Morgan I., Disney M. J., 1994, MNRAS, 268, 393
Ebeling H., Edge A. C., Bohringer H., Allen S. W., Crawford C. S., Fabian A. C., Voges W., Huchra J. P., 1998, MNRAS, 301, 881
Ebeling H., Mullis C. R., Tully R. B., 2002, ApJ, 580, 774
Edge A., Sutherland W., Kuijken K., Driver S., McMahon R., Eales S., Emerson J. P., 2013, The Messenger, 154, 32
Eggen O. J., Lynden-Bell D., Sandage A. R., 1962, ApJ, 136, 748
Ellis R., Allington-Smith J., Smail I., 1991, MNRAS, 249, 184
Feretti L., Fusco-Femiano R., Giovannini G., Govoni F., 2001, A&A, 373, 106
Feretti L., Schuecker P., Böhringer H., Govoni F., Giovannini G., 2005, A&A, 444, 157
Feretti L., Giovannini G., Govoni F., Murgia M., 2012, A&A, 20, 54
Ferrari C., Maurogordato S., Cappi A., Benoist C., 2003, A&A, 399, 813
Forman W., Bechtold J., Blair W., Giacconi R., van Speybroeck L., Jones C., 1981, ApJ, 243, L133
Frye B. L. et al., 2007, ApJ, 665, 921
Fumagalli M. et al., 2012, ApJ, 757, L22
Fumagalli M., Fossati M., Hau G. K. T., Gavazzi G., Bower R., Sun M., Boselli A., 2014, MNRAS, 445, 4335
Giovannini G., Tordi M., Feretti L., 1999, New Astron., 4, 141
Giovannini G., Vacca V., Girardi M., Feretti L., Govoni F., Murgia M., 2013, MNRAS, 435, 518
Girardi M., Bardelli S., Barrena R., Boschin W., Gastaldello F., Nonino M., 2011, A&A, 536, A89
Goto T., Yamauchi C., Fujita Y., Okamura S., Sekiguchi M., Smail I., Bernardi M., Gomez P. L., 2003, MNRAS, 346, 601
Murgia, M.Govoni F., Feretti L., Giovannini G., Böhringer H., Reiprich T. H.2001, A&A, 376, 803
Govoni F., Markevitch M., Vikhlinin A., van Speybroeck L., Feretti L., Giovannini G., 2004, ApJ, 605, 695
Gunn J. E., Gott J. R., III1972, ApJ, 176, 1
Gutierrez K., Krawczynski H., 2005, ApJ, 619, 161
Hopkins A. M., Beacom J. F., 2006, ApJ, 651, 142
Houghton R. C. W., Davies R. L., Dalla Bontà E., Masters R., 2012, MNRAS, 423, 256
Hunter J. D., 2007, Comput. Sci. Eng., 9, 90–95
Iglesias-Páramo J., Boselli A., Cortese L., Vílchez J. M., Gavazzi G., 2002, A&A, 384, 383
Jee M. J. et al., 2015, ApJ, 802, 46
Jee M. J. et al., 2016, ApJ, 817, 179
Jones E. et al., 2001. Available at: http://www.scipy.org/
Kale R. et al., 2015, A&A, 579, A92
Karim A. et al., 2011, ApJ, 730, 61
Kennicutt R. C., Jr, 1998, ARA&A, 36, 189
Kocevski D. D., Ebeling H., Mullis C. R., Tully R. B., 2007, ApJ, 662, 224
Kodama T., Balogh M. L., Smail I., Bower R. G., Nakata F., 2004, MNRAS, 354, 1103
Koyama Y. et al., 2013, MNRAS, 434, 423
La Barbera F., Merluzzi P., Busarello G., Massarotti M., Mercurio A., 2004, A&A, 425, 797
Larson R. B., Tinsley B. M., Caldwell C. N., 1980, ApJ, 237, 692
Lawrence A. et al., 2007, MNRAS, 379, 1599
Le Fèvre O. et al., 2015, A&A, 576, A79
Lemonon L., Pierre M., Hunstead R., Reid A., Mellier Y., Boehringer H., 1997, A&A, 326, 34
Lemze D., Broadhurst T., Rephaeli Y., Barkana R., Umetsu K., 2009, ApJ, 701, 1336
Lemze D. et al., 2013, ApJ, 776, 91
Lilly S. J., Le Fevre O., Hammer F., Crampton D., 1996, ApJ, 460, L1
Lilly S. J. et al., 2007, ApJS, 172, 70
Ly C. et al., 2007, ApJ, 657, 738
Madau P., Dickinson M., 2014, ARAA, 52, 415
Madau P., Ferguson H. C., Dickinson M. E., Giavalisco M., Steidel C. C., Fruchter A., 1996, MNRAS, 283, 1388
Marchesini D., van Dokkum P. G., Förster Schreiber N. M., Natascha M., Franx M., Labbé I., Wuyts S., 2009, ApJ, 701, 1765
Markevitch M., Gonzalez A. H., David L., Vikhlinin A., Murray S., Forman W., Jones C., Tucker W., 2002, ApJ, 567, L27
Marmo C., Bertin E., 2008, in Argyle R. W., Bunclark P. S., Lewis J. R., eds, ASP Conf. Ser. Vol. 394, Astronomical Data Analysis Software and Systems XVII. Astron. Soc. Pac., San Francisco, p. 619
Matsuda Y. et al., 2011, MNRAS, 416, 2041
Maurogordato S. et al., 2008, A&A, 481, 593
McMahon R. G. et al., 2013, The Messenger, 154, 3
Medezinski E., Umetsu K., Okabe N., Nonino M., Molnar S., Massey R., Dupke R., Merten J., 2016, ApJ, 817, 24
Merten J. et al., 2011, MNRAS, 417, 333
Monet D. G. et al., 2003, AJ, 125, 984
Moore B., Katz N., Lake G., Dressler A., Oemler A., 1996, Nature, 379, 613
Muzzin A. et al., 2013, ApJ, 777, 18
Ochsenbein F., Bauer P., Marcout J., 2000, A&A, 143, 23
O'Dea K. P. et al., 2010, ApJ, 719, 1619
Ogrean G. A., Brüggen M., van Weeren R., Röttgering H., Simionescu A., Hoeft M., Croston J. H., 2014, MNRAS, 440, 3416
Okabe N., Smith G. P., 2016, MNRAS, 461, 3794
Okabe N., Takada M., Umetsu K., Futamase T., Smith G. P., 2010, PASJ, 62, 811
Okabe N., Bourdin H., Mazzotta P., Maurogordato S., 2011, ApJ, 741, 116
Owers M. S., Couch W. J., Nulsen P. E. J., Randall S. W., 2012, ApJ, 750, L23
Owers M. S., Randall S. W., Nulsen P. E. J., Couch W. J., David L. P., Kempner J. C., 2011, ApJ, 728, 27
Partridge R. B., Peebles P. J. E., 1967, ApJ, 147, 868
Peng Y.-j. et al., 2010, ApJ, 721, 193
Peng Y.-j., Lilly S. J., Renzini A., Carollo M., 2012, ApJ, 757, 4
Pfrommer C., Springel V., Enßlin T. A., Jubelgas M., 2006, MNRAS, 367, 113
Pierre M., Oukbir J., Dubreuil D., Soucail G., Sauvageot J.-L., Mellier Y., 1997, A&A, 124, 283
Postman M. et al., 2012, ApJS, 199, 25
Pranger F., Böhm A., Ferrari C., Maurogordato S., Benoist C., Höller H., Schindler S., 2014, A&A, 570, A40
Quillen A. C. et al., 2008, ApJS, 176, 39
Reid A. D., Hunstead R. W., Lemonon L., Pierre M. M., 1999, MNRAS, 302, 571
Rettura A. et al., 2010, ApJ, 709, 512
Rines K., Geller M. J., Diaferio A., Kurtz M. J., 2013, ApJ, 767, 15
Roediger E., Brüggen M., Owers M. S., Ebeling H., Sun M., 2014, MNRAS, 443, L114
Salinas R., Richtler T., West M. J., Romanowsky A. J., Lloyd-Davies E., Schuberth Y., 2011, A&A, 528, A61
Schechter P., 1976, ApJ, 203, 297
Schlafly E. F., Finkbeiner D. P., 2011, ApJ, 737, 103
Shanks T. et al., 2015, MNRAS, 451, 4238
Shioya Y. et al., 2008, ApJS, 175, 128
Skrutskie M. F. et al., 2006, AJ, 131, 1163
Sobral et al., 2009, MNRAS, 398, 75

Sobral D., Best P. N., Smail I., Geach J. E., Cirasuolo M., Garn T., Dalton G. B., 2011, MNRAS, 411, 675
Sobral D., Best P. N., Matsuda Y., Smail I., Geach J. E., Cirasuolo M., 2012, MNRAS, 420, 1926
Sobral D., Smail I., Best P. N., Geach J. E., Matsuda Y., Stott J. P., Cirasuolo M., Kurk J., 2013, MNRAS, 428, 1128
Sobral D., Best P. N., Smail I., Mobasher B., Stott J., Nisbet D., 2014, MNRAS, 437, 3516
Sobral D., Stroe A., Dawson W. A., Wittman D., Jee M. J., Röttgering H., van Weeren R. J., Brüggen M., 2015, MNRAS, 450, 630
Stevens J. A. et al., 2003, Nature, 425, 264
Stroe A., Sobral D., 2015, MNRAS, 453, 242
Stroe A., Sobral D., Röttgering H. J. A., van Weeren R. J., 2014a, MNRAS, 438, 1377
Stroe A., Harwood J. J., Hardcastle M. J., Röttgering H. J. A., 2014b, MNRAS, 445, 1213
Stroe A. et al., 2015a, MNRAS, 450, 646
Stroe A., Oosterloo T., Röttgering H. J. A., Sobral D., van Weeren R., Dawson W., 2015b, MNRAS, 452, 2731
Umeda K. et al., 2004, ApJ, 601, 805
van der Walt S., Colbert S. C., Varoquaux G., 2011, Comput. Sci. Eng., 13, 2
van Weeren R. J., Röttgering H. J. A., Brüggen M., Hoeft M., 2010, Science, 330, 347
van Weeren R. J., Brüggen M., Röttgering H. J. A., Hoeft M., 2011, MNRAS, 418, 230
van Weeren R. J., Röttgering H. J. A., Intema H. T., Rudnick L., Brüggen M., Hoeft M., Oonk J. B. R., 2012, A&A, 546, A124
van Weeren R. J. et al., 2013, ApJ, 769, 101
van Weeren R. J. et al., 2016, ApJ, 818, 204
van Weeren R. J. et al., 2017, Nature Astron., in press
Vazza F., Dolag K., Ryu D., Brunetti G., Gheller C., Kang H., Pfrommer C., 2011, MNRAS, 418, 960
Verheijen M., van Gorkom J. H., Szomoru A., Dwarakanath K. S., Poggianti B. M., Schiminovich D., 2007, ApJ, 668, L9
Wright E. L., 2006, PASP, 118, 1711
Zacharias N., Finch C. T., Girard T. M., Henden A., Bartlett J. L., Monet D. G., Zacharias M. I., 2013, AJ, 145, 44
Ziparo F., Braglia F. G., Pierini D., Finoguenov A., Böhringer H., Bongiorno A., 2012, MNRAS, 420, 2480
Zitrin A. et al., 2015, ApJ, 801, 44
ZuHone J. A., Markevitch M., Johnson R. E., 2010, ApJ, 717, 908

APPENDIX A: CLUSTER PROPERTIES

Below, we describe each cluster from our sample in detail. As in Table 1, the targets are separated in relaxed and merging, and presented in increasing redshift order.

A1 Relaxed

A1.1 A1689

A1689 is an X-ray bright (Böhringer et al. 2007), relaxed, massive ($M_{200} = 2.0^{+0.5}_{-0.3} \times 10^{14}\,M_\odot$), strong lensing cluster at $z = 0.183$, which hosts the largest known *Einstein* partial ring (Coe et al. 2010). The relaxed nature of the cluster is also supported by spectroscopic data, which indicates the cluster is concentrated, with minimal infall on to the cluster (Lemze et al. 2009). Balogh et al. (2002) performed a spectroscopic Hα analysis and found that relative to the field and after accounting for the different spiral fraction, the cluster Hα LF is lower by ∼50 per cent.

A1.2 A963

Relaxed cluster A963 ($z = 0.206$) has an almost perfect *Einstein* ring around its brightest cluster galaxy (BCG; Ellis, Allington-Smith & Smail 1991). The cluster has a weak lensing mass of $M_{200} = 7.6^{+1.5}_{-1.3} \times 10^{14}\,M_\odot$ (Okabe & Smith 2016) and an X-ray luminosity $L_{X,0.1-2.4\,keV} \sim 6 \times 10^{44}$ erg s^{-1} (Okabe et al. 2010). Verheijen et al. (2007) did pioneering H I work, detecting neutral hydrogen in field galaxies and blue galaxies at the cluster outskirts, however not having any detection for the counterparts located at the cluster core. Driver et al. (1994) found that the cluster hosts an high number of dwarf galaxies compared to the field.

A1.3 A1423

The relaxed cluster A1423 ($z = 0.213$) has a low weak lensing mass of $M_{200} = 4.6^{+1.2}_{-1.0} \times 10^{14}\,M_\odot$ (Okabe & Smith 2016). As part of the CLASH programme (Postman et al. 2012), the cluster was also found to be strong lensing (Zitrin et al. 2015).

A1.4 A2261

The borderline relaxed $z = 0.224$ A2261 cluster has a weak lensing mass of $M_{200} = 12.75^{+2.3}_{-1.5} \times 10^{14}\,M_\odot$ (Okabe & Smith 2016). The cluster hosts one of the largest BCGs known. Coe et al. (2012) suggest that the cluster was formed at $1.7 < z < 2.9$.

A1.5 A2390

A2390 ($z = 0.228$) is a relaxed cluster with a weak lensing mass of $M_{200} = 11.1^{+1.9}_{-1.7} \times 10^{14}\,M_\odot$ (Okabe & Smith 2016). This X-ray luminous cluster ($L_{X,0.1-2.4\,keV} \sim 12.7 \times 10^{44}$ erg s^{-1}, Okabe et al. 2010), hosts diffuse radio emission with irregular morphology (sharp edges towards south and east and filaments towards the north), associated with sloshing around the central, dominant galaxy (mini-halo Bacchi et al. 2003). Abraham et al. (1996) concluded that only 5 per cent of the cluster members have SF at levels higher than typical spirals, indicating that the cluster has been accreting field galaxies for >8 Gyr whose SF has been promptly truncated in the infall process.

A1.6 Z2089

Z2089 is a relaxed cluster at $z = 0.2343$ with $L_{X,0.1-2.4\,keV} \sim 6.8 \times 10^{44}$ erg s^{-1} (Ebeling et al. 1998) and weak lensing mass $M_{200} \sim 5 \times 10^{14}\,M_\odot$ (Dahle 2006). The cluster has a prominent central red source, which possibly hosts dusty AGN (Quillen et al. 2008).

A1.7 RXJ2129

RXJ2129.6+0005 (RXJ2129) is a relatively bright, relaxed cluster at $z = 0.235$ (Böhringer et al. 2004), which hosts a mini-halo around the radio source at the centre of the cluster (Kale et al. 2015). The cluster X-rays are elongated in the NW–SW direction (O'Dea et al. 2010; Kale et al. 2015). The cluster has a weak lensing mass of $M_{200} = 5.3^{+1.8}_{-1.4} \times 10^{14}\,M_\odot$ (Okabe et al. 2010).

A1.8 RXJ0437

RX J0437.1+0043 (RXJ0437) is a relaxed cluster ($z = 0.285$, Böhringer et al. 2004) with a weak lensing mass $M_{200} \sim 5 \times 10^{14}\,M_\odot$ (Dahle 2006). The elliptical X-ray morphology is consistent with a relaxed state (Feretti et al. 2005).

A2 Merging

A2.1 A545

A545 is at a redshift of 0.154 and has an X-ray luminosity of $L_{X,0.1-2.4\,keV} \sim 5.05 \times 10^{44}$ erg s^{-1} (Böhringer et al. 2004). Barrena et al. (2011) performed a detailed spectroscopic and X-ray analysis of the cluster and find an extremely complex and disturbed morphology with at least three subclusters and no dominant galaxy. At the centre of the cluster, there exists a 'star pile', an extended low-surface brightness feature with three nuclei, which Salinas et al. (2011) interpret as the remnant of a tidally stripped galaxy or galaxies. Böhringer et al. (2004) find evidence for an X-ray shock coinciding with the northern edge of the regular, centrally located radio halo (which was studied in detail by Bacchi et al. 2003). Barrena et al. (2011) interpreted their data as indicative of a merger happening in two directions, within the plane of the sky. Based on their spectra, Barrena et al. (2011) calculated a mass of about $M \sim (11–18) \times 10^{14}\,M_{\odot}$.

A2.2 A3411

Based on X-ray data, A3411 ($z = 0.169$; Ebeling, Mullis & Tully 2002) is a complex merging cluster which is possibly interacting with the nearby A3412 and hosts both a radio halo and a 1.9-Mpc radio relic towards the south-east of the cluster (Giovannini et al. 2013; van Weeren et al. 2013). X-ray and radio data indicate that the relic is possibly formed by a weak shock ($M < 1.3$) re-accelerating fossil plasma from a nearby radio AGN (van Weeren et al. 2017). The emerging scenario is that of a binary 1:1 merger, happening in the plane of the sky in the NW–SE direction and observed 1 Gyr after core passage (van Weeren et al. 2017). The northern subcluster (A3411) survived the collision, while the southern subcluster (A3412) was stripped of its gas during the merger (van Weeren et al. 2017). Based on a dynamical analysis, van Weeren et al. (2017) estimate a mass of $14^{+4}_{-3} \times 10^{14}$ and $18^{+5}_{-4} \times 10^{14}\,M_{\odot}$ for A3411 and A3412, respectively.

A2.3 A2254

Based on an optical and X-ray analysis, Girardi et al. (2011) classify A2254 ($z = 0.178$; Govoni et al. 2001) as a binary, post-merger cluster, which hosts a radio halo (Giovannini, Tordi & Feretti 1999). Based on spectroscopy, Girardi et al. (2011) estimate the total mass of the system to be about $(15–29) \times 10^{14}\,M_{\odot}$. The relative line-of-sight (LOS) velocity of ∼3000 km s^{-1} and the projected linear distance between the two subclusters of ∼0.5 Mpc are consistent with a young merger, with core passage happening <0.5 Gyr ago.

A2.4 CIZA J2242.8+5301

CIZA J2242.8+5301 ('Sausage', $z = 0.188$; Kocevski et al. 2007; Dawson et al. 2015) is a merging galaxy cluster hosting double, symmetric radio-detected shocks perpendicular to the merger axis (van Weeren et al. 2010). Radio modelling and X-ray data indicate a Mach number $M \sim 3$ for the main 1.4-Mpc shock (Akamatsu & Kawahara 2013; Ogrean et al. 2014; Stroe et al. 2014a), however some studies find a higher Mach number of ∼4.5 (van Weeren et al. 2010; Donnert et al. 2016). The cluster is consistent with a massive post-core passage merger between two clusters of similar masses $M_{200} = 11.0^{+3.7}_{-3.2} \times 10^{14}$ and $9.8^{+3.8}_{-2.5} \times 10^{14}\,M_{\odot}$ (weak lensing analysis consistent with dynamical analysis; Dawson et al. 2015; Jee et al. 2015), with the merger happening about 0.5–1.0 Gyr ago (van Weeren et al. 2011; Stroe et al. 2014b). The cluster was found to host a significant overdensity of Hα emitters, which are more massive, more H I gas rich and more SF than their field counterparts (Stroe et al. 2014a, 2015a,b) and have evidence for outflows from supernovae and AGN activity (from spectroscopy, Sobral et al. 2015).

A2.5 A115

Forman et al. (1981) found that A115 at $z = 0.1971$ has a double X-ray peak, consistent with two subclusters with substantial off-axis motion (Gutierrez & Krawczynski 2005). The X-ray luminosity of the cluster is $L_{X,0.1-2.4\,keV} \sim 9 \times 10^{44}$ erg s^{-1}, while its weak lensing mass is $6.7^{+3.2}_{-2.1} \times 10^{14}\,M_{\odot}$ (Okabe & Smith 2016). Barrena et al. (2007b) performed a spectroscopic study of A115 and found that the galaxies in the northern, less massive subcluster are experiencing higher SF activity compared to the southern subcluster. They propose a pre-merging scenario where the two subclusters are colliding at a LOS velocity of 1600 km s^{-1} and will cross within 0.1 Gyr. However, this scenario is not fully consistent with the presence of arc-like diffuse emission extended over 2 Mpc (Govoni et al. 2001), cospatial with a $M \sim 1.8$ X-ray shock (Botteon et al. 2016), which indicates the presence of a merger shock perpendicular to the merger axis.

A2.6 A2163

A2163 is an exceptionally hot, luminous, massive ($M_{200} = 29.0^{+4.6}_{-5.8} \times 10^{14}\,M_{\odot}$) merging cluster at $z = 0.203$ (Feretti et al. 2001; Okabe et al. 2011). The optical analysis performed by Maurogordato et al. (2008) reveals a complex merging scenario: the cluster has a main bi-modal central component, a northern component as well as two other substructures. Maurogordato et al. (2008) infer the main clump has undergone a recent merger in the last 0.5 Gyr along the NW–SW direction, probably with a non-zero impact parameter (Okabe et al. 2011), with the northern component infalling into the cluster. A weak lensing analysis indicated that the two main clump components have a mass ratio of 1:8 (Okabe et al. 2011). Okabe et al. (2011) also found an offset between the X-ray distribution and the galaxy density, attributed to ram pressure stripping of gas away from the dark matter host. The cluster also hosts a giant radio halo, indicative of increased turbulence in the main clump (Feretti et al. 2001).

A2.7 A773

A773 ($z = 0.217$) is a binary merging cluster with ∼4:1 mass ratio, merging in the NE–SW direction, with a weak lensing mass of $M_{200} = 10.2^{+1.5}_{-1.3} \times 10^{14}\,M_{\odot}$ (Okabe & Smith 2016). Govoni et al. (2004) found that one of the two galaxy subclumps coincides with the centre of the X-ray emission, while a radio halo is located in the cool region between the two subclusters. Barrena et al. (2007a), using spectroscopic data, concluded the cluster is in an advanced stage of merging with an impact velocity of ∼2300 km s^{-1}.

A2.8 1RXS J0603.3+4214

1RXS J0603.3+4214 ('Toothbrush' cluster, $z = 0.225$) was discovered as a merging cluster with diffuse radio emission in the form of at least one 1.9-Mpc, linear shock perpendicular to the merger axis and a halo by van Weeren et al. (2012). Radio observations indicate a Mach number of ∼2.8, in tension with X-ray observations which predict a much lower value of ∼1.2 (van Weeren et al. 2016). The merger scenario is complicated, with two massive colliding clumps with a mass ratio of 3:1 ($M_{200} = 6.3^{+2.2}_{-1.6} \times 10^{14}\,M_\odot$ and $M_{200} = 2.0^{+1.2}_{-0.7} \times 10^{14}\,M_\odot$), as well as 1–2 smaller clumps participating in the merger (weak lensing analysis, Jee et al. 2016). This view is roughly consistent with hydrodynamical simulations by Brüggen, van Weeren & Röttgering (2012) who also find a complicated merger scenario necessary and place the main clump core passage at about 2 Gyr ago. The cluster was found to have a similar density of Hα emitters as field galaxies at the same redshift (Stroe et al. 2014a, 2015a).

A2.9 A2219

A2219 (Okabe et al. 2010) is one of the hottest, most X-ray luminous clusters known (Canning et al. 2015). A post-merger cluster at $z = 0.2256$ with weak lensing mass of $M_{200} = 10.9^{+2.2}_{-1.8} \times 10^{14}\,M_\odot$ (Okabe & Smith 2016), A2219 hosts a radio halo with regular and symmetric structure (Bacchi et al. 2003). Boschin et al. (2004) performed a detailed spectroscopic study of A2219 and found a high velocity dispersion, from which they derive a total mass of $\sim 28 \times 10^{14}\,M_\odot$. Their data indicate a merger axis on the SE–NW direction, inclined at about 45° from the plane of the sky Boschin et al. (2004). Canning et al. (2015) find two shocks and a cold front perpendicular on the merger axis, coincident with the edges of the radio halo, and estimate a times since core passage of about ∼0.26 Gyr.

A2.10 A1300

A1300 is a hot, luminous (Böhringer et al. 2004) post-merger cluster at $z = 0.3072$ (Pierre et al. 1997; Ziparo et al. 2012). The cluster hosts a halo (Reid et al. 1999), and has evidence for a $M = 1.2$ shock from X-ray data (Ziparo et al. 2012) coincident with a radio relic towards the south-west edge. Comparison with simulations indicates that ∼3 Gyr have passed since core passage, to form a system with $M_{200} \sim 6 \times 10^{14}\,M_\odot$ (Ziparo et al. 2012).

A2.11 A2744

A2744 ($z = 0.308$) is an extremely disturbed, complex and young merging cluster with high X-ray luminosity (Govoni et al. 2001) and large weak lensing mass $M_{200} = 20.6 \pm 4.2 \times 10^{14}\,M_\odot$ (Medezinski et al. 2016). The cluster hosts at least four substructures with mass ratios approximately 2:1:1:1. Merten et al. (2011) propose a scenario of a simultaneous double merger happening 0.12–0.15 Gyr ago, one bullet-like merger in the NE–SW and the other in the NW–SE direction. Owers et al. (2012) find galaxies with trails of SF which are affiliated with the Bullet-like subcluster and the X-ray shock.

This paper has been typeset from a TEX/LATEX file prepared by the author.